

## Article

# Manganese, Fluorine, and Nitrogen Co-Doped Bronze Titanium Dioxide Nanotubes with Improved Lithium-Ion Storage Properties

Denis P. Opra <sup>1,\*</sup>, Sergey L. Sinebryukhov <sup>1</sup>, Evgeny B. Modin <sup>2</sup>, Alexander A. Sokolov <sup>1</sup>, Anatoly B. Podgorbunsky <sup>1</sup>, Albert M. Ziatdinov <sup>1</sup>, Alexander Y. Ustinov <sup>1</sup>, Vitaly Y. Mayorov <sup>1</sup> and Sergey V. Gnedenkov <sup>1</sup>

<sup>1</sup> Institute of Chemistry, Far Eastern Branch of the Russian Academy of Sciences, 690022 Vladivostok, Primorsky Krai, Russia

<sup>2</sup> CIC NanoGUNE BRTA, 20008 Donostia-San Sebastian, Spain

\* Correspondence: dp.opra@ich.dvo.ru; Tel.: +7-423-2311889; Fax: +7-423-2312590

**Abstract:** Because of the unique crystal framework, bronze TiO<sub>2</sub> (or TiO<sub>2</sub>(B)) is considered the prospective choice for high-performance lithium-ion battery anodes. Nevertheless, TiO<sub>2</sub>(B) requires efficient modification, e.g., suitable doping with other elements, to improve the electronic properties and enhance the stability upon insertion/extraction of guest ions. However, due to the metastability of TiO<sub>2</sub>(B), doping is challenging. Herein, for the first time, TiO<sub>2</sub>(B) co-doped with Mn, F, and N were synthesized through a successive method based on a hydrothermal technique. The prepared doped TiO<sub>2</sub>(B) consists of ultrathin nanotubes (outer diameter of 10 nm, wall thickness of 2–3 nm) and exhibits a highly porous structure (pore volume of up to 1 cm<sup>3</sup> g<sup>-1</sup>) with a large specific surface area near 200 m<sup>2</sup> g<sup>-1</sup>. The incorporation of Mn, F, and N into TiO<sub>2</sub>(B) expands its crystal lattice and modifies its electronic structure. The band gap of TiO<sub>2</sub>(B) narrows from 3.14 to 2.18 eV upon Mn- and N-doping and electronic conductivity improves more than 40 times. Doping with fluorine improves the thermal stability of TiO<sub>2</sub>(B) and prevents its temperature-induced transformation into anatase. It was found that the diffusivity of Li is about two times faster in doped TiO<sub>2</sub>(B). These properties make Mn, F, and N co-doped TiO<sub>2</sub>(B) nanotubes promising for application as high-performance anodes in advanced lithium-ion batteries. In particular, it possesses a good reversible capacity (231.5 mAh g<sup>-1</sup> after 100 cycles at 70 mA g<sup>-1</sup>) and prominent rate capability (134 mAh g<sup>-1</sup> at 1500 mA g<sup>-1</sup>) in the half-cell configuration. The (Mn, F, N)-doped TiO<sub>2</sub>(B) possesses a remarkable low-temperature Li storage performance, keeping 70% of capacity at -20 °C and demonstrating potentialities to be employed in full-cell configuration with LiMn<sub>2</sub>O<sub>4</sub> cathode delivering a reversible capacity of 123 and 79 mAh g<sup>-1</sup> at 35 and 1500 mA g<sup>-1</sup>, respectively, at a voltage of ~2.5 V. This research underlies that regulation of electronic and crystal structure is desired to uncover capabilities of nanoparticulate TiO<sub>2</sub>(B) for electrochemical energy storage and conversion.

**Keywords:** TiO<sub>2</sub>(B); nanotubes; co-doping; electronic properties; lithium-ion batteries



**Citation:** Opra, D.P.; Sinebryukhov, S.L.; Modin, E.B.; Sokolov, A.A.; Podgorbunsky, A.B.; Ziatdinov, A.M.; Ustinov, A.Y.; Mayorov, V.Y.; Gnedenkov, S.V. Manganese, Fluorine, and Nitrogen Co-Doped Bronze Titanium Dioxide Nanotubes with Improved Lithium-Ion Storage Properties. *Batteries* **2023**, *9*, 229. <https://doi.org/10.3390/batteries9040229>

Academic Editors: Johan E. ten Elshof and Irina A. Stenina

Received: 14 January 2023

Revised: 27 March 2023

Accepted: 14 April 2023

Published: 17 April 2023



**Copyright:** © 2023 by the authors. Licensee MDPI, Basel, Switzerland. This article is an open access article distributed under the terms and conditions of the Creative Commons Attribution (CC BY) license (<https://creativecommons.org/licenses/by/4.0/>).

## 1. Introduction

Titanium dioxide is characterized by unique physical and chemical properties along with non-toxicity, abundance, environmental benignity, and economical production. TiO<sub>2</sub>, first mass-produced a century ago, is considered to be an important substance for preparing materials with valuable qualities to use in diversified areas of industry. Because of its whiteness and brightness, TiO<sub>2</sub> is allowed as a pigment and gloss agent for paints, cosmetics, hygienic products, foods, papers, plastics, pharmaceuticals, etc. [1,2]. Due to resistance to ultraviolet radiation, titanium dioxide is applied as a UV filtering ingredient in sunscreens protecting against the sun's light that may affect a person's skin [3,4]. Discovering the

photoassisted electrolysis of water by TiO<sub>2</sub> resulted in its applications for the decontamination of aqueous media via the degradation of organic wastes into harmless substances and hydrogen generation through water splitting [5,6]. Over the past decades, TiO<sub>2</sub> has been intensively studied to be used in a range of innovative technologies, including gas sensors [7,8], biomedical applications [9,10], superhydrophilic surfaces [11,12], memory devices [13,14], solar cells [15,16], dilute magnetic semiconductors [17,18], and metal-ion batteries [19,20].

TiO<sub>2</sub> has thirteen polymorphic forms: rutile (tetragonal,  $P4_2/mnm$ ), anatase (tetragonal,  $I4_1/amd$ ), brookite (orthorhombic,  $Pbca$ ), bronze-type TiO<sub>2</sub>(B) (monoclinic,  $C2/m$ ), columbite-like TiO<sub>2</sub>(II) (orthorhombic,  $Pbcn$ ), hollandite-structured TiO<sub>2</sub>(H) (tetragonal,  $I4/m$ ), ramsdellite-type TiO<sub>2</sub>(R) (orthorhombic,  $Pbnm$ ), TiO<sub>2</sub>(OI) (orthorhombic,  $Pbca$ ), cotunnite-like TiO<sub>2</sub>(OII) (orthorhombic,  $Pnma$ ), baddeleyite-like TiO<sub>2</sub>(MI) (monoclinic,  $P2_1/c$ ), fluorite- (cubic,  $Fm\bar{3}m$ ) and pyrite-structured (cubic,  $Pa\bar{3}$ ) phases, tridymite-type TiO<sub>2</sub> (hexagonal,  $P6_3/mmc$ ) [21–24]. Nevertheless, at atmospheric pressure, titanium dioxide can exist just in the first four crystalline polymorphs, whereas other ones are high-pressure structures. Among these four phases, bronze TiO<sub>2</sub> is of most interest to the battery's application because of its structural singularities, such as reduced crystallographic density and open-framework structure with channels in both  $b$  and  $c$  directions providing intercalation sites and facilitating diffusion paths (so-called pseudocapacitive (de-)insertion behavior) [25–27]. The redox chemistry of TiO<sub>2</sub>(B) in lithium-ion batteries is based on a (de-)intercalation mechanism and driven by a Ti<sup>4+</sup>/Ti<sup>3+</sup> couple operating at ~1.5 V [28]. When used as anode-active material the elevated operating potential of TiO<sub>2</sub>(B) decreases the energy density of the battery as opposed to that based on conventional graphite (~0.1 V vs. Li/Li<sup>+</sup> [29]). In contrast, carbonate-based electrolytes almost do not decompose at the TiO<sub>2</sub>(B) surface (because its potential lies within their electrochemical window [29,30]), which is critical for high-performance materials offering high current densities. In contrast to Li<sub>4</sub>Ti<sub>5</sub>O<sub>12</sub> (~1.55 V vs. Li/Li<sup>+</sup>), studied for the same reasons, TiO<sub>2</sub>(B) has almost twice higher the lithium storage capacity of 335 mAh g<sup>-1</sup> [31]. Other materials based on conversion and (de-)alloying reactions offering higher energy densities suffer from dramatic volume changes upon (de-)lithiation (e.g., about 150, 300, and 400% for Sb, Sn, and Si) and/or irreversibility (chemistry of conversion-type materials is changed during initial lithiation), which limits their cyclic performance [32,33]. On the contrary, the volume expansion of lithiated TiO<sub>2</sub> did not exceed 4% which is even less than for graphitic materials (9–13%) [34,35]. Unfortunately, TiO<sub>2</sub>(B) which is an  $n$ -type semiconductor with a wide band gap of 3.09–3.23 eV [36,37] possesses poor conductive properties.

The conductivity of TiO<sub>2</sub>(B) can be adjusted by doping with appropriate ions or atoms. Additionally, doping can expand the crystal lattice of TiO<sub>2</sub>(B) reducing the volume changes upon (de)insertion of lithium ions. However, due to its metastable nature and low thermodynamically stable temperature, TiO<sub>2</sub>(B) doping is challenging and accompanied by the formation of other phases (most often anatase) as undesirable by-products. For the same reason (transition of bronze phase to anatase occurs at temperatures below 500 °C), it is impossible to address the TiO<sub>2</sub>(B) conductivity issues through the construction of carbon-coated composite structures (carbonization takes place at high temperatures around 700–900 °C) that is most often used strategy for electrode materials. The reported dopants, which show a more or less favorable effect on the electrical conductivity and, hence, the performance of TiO<sub>2</sub>(B) in lithium-ion batteries (LIBs), including Fe [38], Ca [39], Cu [40], Ni [41], V [42], Co/V [43], P [44], N [45], N/B [46], Nb [47], C [48,49], and Na [50].

Besides the aforementioned, it is well recognized that the conductive properties demonstrate the particle size-dependent behavior, hence, the control of morphology is strongly required to obtain the high-performance TiO<sub>2</sub>(B) intercalation host for LIBs. Hydro(solvo)thermal synthesis is a suitable method to prepare the nanocrystalline TiO<sub>2</sub>(B), which allows modifying (doping or hybridization) it at a time via a one-step process [51–53].

Within the present study we have fabricated, for the first time, TiO<sub>2</sub>(B) co-doped with Mn, F, and N having nanotubular morphology via a one-stage hydrothermal method. The

synergistic effect of Mn, F, and N doping increases the electronic conductivity and expands the crystal lattice of  $\text{TiO}_2(\text{B})$ . When tested as an anode for lithium-ion batteries, co-doped  $\text{TiO}_2(\text{B})$  exhibit enhanced electrochemical performance with both improved cyclability and rate capability.

## 2. Materials and Methods

### 2.1. Materials Synthesis

Mn, F, and N co-doped titanium dioxide structures were prepared by a successive method involving hydrothermal treatment of precursors, cation exchange process, and calcination. In a typical procedure, 0.4 g anatase with an average particle size of 15 nm (99.7%; Alfa Aesar, Ward Hill, MA, USA), manganese(II) nitrate hexahydrate ( $\text{Mn}(\text{NO}_3)_2 \cdot 6\text{H}_2\text{O}$ , >99%; Unichim, St. Petersburg, Russia) and ammonium hydrogen fluoride ( $\text{NH}_4\text{HF}_2$ , >98%, Unichim, Russia) in certain amounts were stirred together with 40 mL 14 M aqueous solution of sodium hydroxide ( $\text{NaOH}$ , >99%, Ekos-1, Moscow, Russia) and transferred into the 50 mL polytetrafluoroethylene autoclave. The reaction was carried out for 48 h at 160 °C. After cooling at room temperature, the precipitate (based on sodium titanate(s)) was separated using an Eppendorf 5804R centrifuge. Then, the product was rinsed in 0.05 M  $\text{HNO}_3$  solution for a few days to rid of the  $\text{Na}^+$  ions through a cation-exchange reaction. At last, the obtained Mn-, F-, and N-containing protonated titanate (single or polyphase) was washed in deionized water until the neutral pH, dried, and heat treated at 350 °C for 3 h. To examine the doping degree effect, manganese was added in the following concentrations: 2 at.% (TO-Mn/F/N-02), 4 at.% (TO-Mn/F/N-04), and 6 at.% (TO-Mn/F/N-06); where TO is a short-term representation of  $\text{TiO}_2$ . The fluorinating/nitriding agent was added in excess amounts at a Mn to F ratio of 1 to 3. Undoped titanium dioxide was synthesized via the same procedure but without  $\text{Mn}(\text{NO}_3)_2 \cdot 6\text{H}_2\text{O}$  and  $\text{NH}_4\text{HF}_2$ .

### 2.2. Characterization

The morphology and composition of materials were observed by scanning electron microscopy (SEM) on a Thermofisher Helios 450S, high-resolution transmission (HRTEM) and scanning transmission electron microscopy (STEM), and selected area electron diffraction (SAED) on a Thermofisher Titan 60–300 coupled with energy-dispersive X-ray spectroscopy (EDX) attachment. Electron energy loss spectroscopy (EELS) measurements were done using Gatan Quantum 965. Low-temperature (77 K) nitrogen adsorption–desorption experiments were carried out using a Quantachrome Autosorb iQ analyzer to estimate the porosity and specific surface area of samples (using the non-local density functional theory (NLDFT)). The chemical state of elements was investigated by X-ray photoelectron spectroscopy (XPS) using a monochromatic  $\text{MgK}\alpha$  ( $h\nu = 1253.6$  eV) X-ray source on a SPECS spectrometer equipped with a Phoibos-150 hemispherical energy analyzer. The binding energies were determined by referencing XPS data to the C 1s emission of ubiquitous carbon contaminations at 285 eV. To analyze the phase composition of materials and changes in the crystalline structure of phases, the X-ray powder diffraction studies (XRD, Rigaku SmartLab) were performed using  $\text{CuK}\alpha$  ( $\lambda = 1.5418$  Å). Measurements were conducted in the Bragg-Brentano geometry ( $\theta/2\theta$  mode) with  $2\theta$  step of  $0.01^\circ$ . Diffrac EVA software (ver. 6) from Bruker (Billerica, MA, USA) and PDF2 database (2015) were applied for phase identification. To calculate lattice parameters the Rietveld method (in a  $2\theta$  range of  $7\text{--}83^\circ$ ) was applied. For the refinement of structures, the JANA2006 program [54] was used. The optical properties and changes in the electronic structure of materials were studied using a Shimadzu UV2600 UV-vis spectrophotometer between the wavelengths of 200 and 800 nm.  $\text{BaSO}_4$  was applied as a reflectance standard. To detect and identify the paramagnetic species in materials electron paramagnetic resonance (EPR) studies were conducted on a JEOL JES-X330 spectrometer in the X- and Q-band regions using 2.0 mW microwave power and 100 kHz modulation frequency. The integral intensities and g-factors of the EPR lines were calibrated, respectively, by the integral intensity and the value  $g = 2.002293 \pm 0.000003$  of the conduction electron spin resonance signal of Li

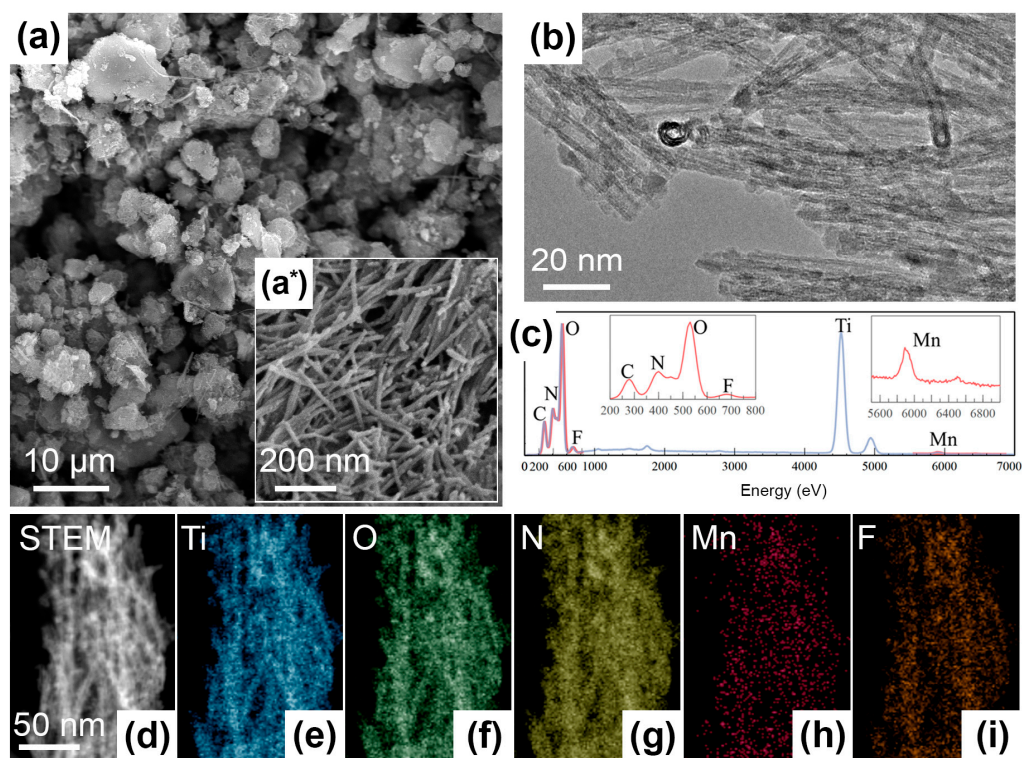
nanoparticles in the reference LiF:Li sample. The conductivity was investigated using a measuring complex from Solartron consisting of SI 1260 impedance/gain-phase analyzer and a 1296 dielectric interface. Measurements were carried out in a frequency range of 1 Hz–20 MHz with an AC amplitude of 0.4 V. Fitting of impedance spectra was performed using an equivalent electrical circuit (EEC) approach with Zview software (ver. 3.5 g) from Scribner Associates (Southern Pines, NC, USA).

### 2.3. Electrochemical Measurements

The electrochemical performance of samples was examined using two-electrode El-Cell ECC-STD laboratory cells and CR2025 coin-type cases in both half-cell and full-cell configuration with metallic lithium or  $\text{LiMn}_2\text{O}_4$  (Sigma-Aldrich, St. Louis, MO, USA), respectively, as a counter/reference electrode. For cell assembly, an argon-filled dried ( $\text{O}_2$ ,  $\text{H}_2\text{O} < 1$  ppm) glove box from Viletek (Moscow, Russia) was used. The electrode was fabricated by the Doctor Blade method spreading a slurry composed of 87 wt.%  $\text{TiO}_2(\text{B})$  or  $\text{LiMn}_2\text{O}_4$  as an active material and 13 wt.% Tuball Bat NMP (0.4%; OCSiAl, Russia) as a conductive/binder agent in 1-Methyl-2-pyrrolidinone on a copper or aluminium foil. After drying the electrode was pressed at  $800 \text{ kg cm}^{-2}$  and treated under vacuum at  $110 \text{ }^\circ\text{C}$  for 12 h. The electrode mass loading in the range of  $2\text{--}4 \text{ mg cm}^{-2}$  was achieved. The mass of anode to cathode in  $\text{TiO}_2(\text{B})/\text{LiMn}_2\text{O}_4$  full-cell was balanced at a ratio of 1:1.5. The electrolyte was a 1 M  $\text{LiPF}_6$  solution in a mixture (1:1 by volume) of ethylene carbonate and dimethyl carbonate (Merck, Rahway, NJ, USA) for experiments under ambient conditions or 1 M solution of  $\text{LiClO}_4$  in the mixture (84:16, vol. ratio) of propylene carbonate and 1,2-dimethoxyethane (Ekotekh, Chernogolovka, Russia) for low-temperature tests. Celgard 2325 microporous triple-layer membrane was used as a separator. Electrochemical characterization was carried out using a Solartron 1400 system within the potential range of 1–3 V ( $\text{TiO}_2(\text{B})$ ) or 3–4.5 V ( $\text{LiMn}_2\text{O}_4$ ) in the half-cell configuration and 2.1–2.9 V in the full-cell assembly. Cyclic voltammograms (CV) were registered at a potential scan rate of  $0.1 \text{ mV s}^{-1}$ . Charge/discharge tests were conducted in a galvanostatic mode at different current densities. In the case of half-cell assembly, during the discussions, the charge designates a lithiation process, while the discharge implies delithiation. Electrochemical impedance spectra (EIS) were collected with an AC amplitude of 10 mV over the frequency range of 1 MHz to 0.1 Hz. At least four cells were applied for each test.

### 3. Results and Discussion

Due to the same synthesis conditions, the morphology of all obtained materials is similar. Figure 1(a,a\*) depict the SEM micrographs of TO-Mn/F/N-04 as an example. For other samples, these data are presented in the Supplementary Materials in Figure S1. From SEM-imaging the prepared products possess a multimodal dispersion and uniformity of particle size distribution which are valuable parameters for functional materials, including electrodes for batteries. They consist of one-dimensional (1D) elongated cylindrical nanoobjects. Under deeper insight using STEM-mode (Figure 1b), it can be seen that these objects are nanotubes. The diameter of tubes is around 10 nm and the length could be up to several hundred nanometers. The nanotube's wall thickness was measured as 2–3 nm. In general, hollow nanostructures provide benefits for the transfer of charge carriers or transportation of substances, e.g., drugs.



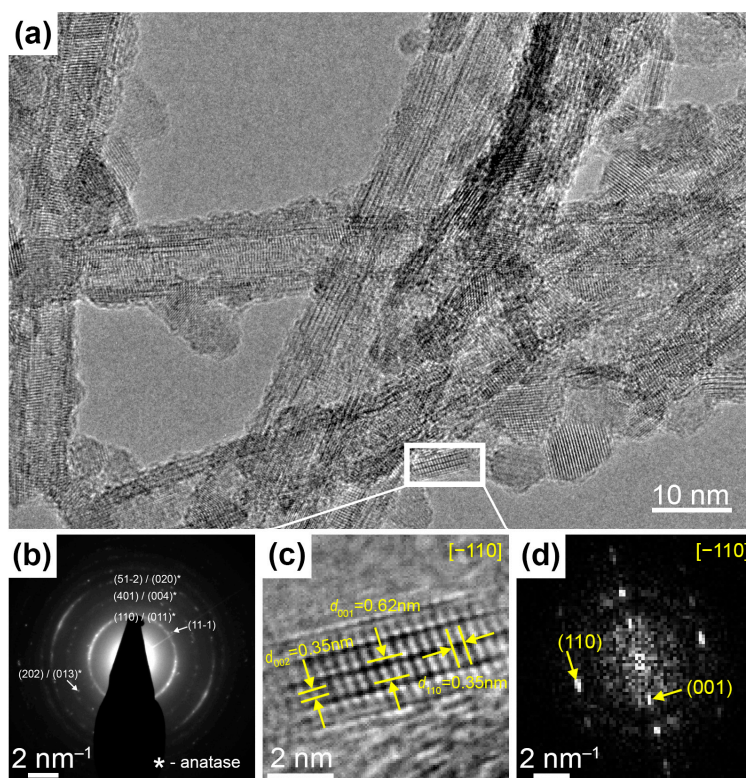
**Figure 1.** Morphology and elemental analysis for Mn, F, N co-doped  $\text{TiO}_2$ : (a,a\*) SEM- and (b) STEM-images of the TO-Mn/F/N-04 sample, (c) EDX-spectrum and (d–i) elemental mapping for the TO-Mn/F/N-02.

Figure 1c depicts the EDX-spectrum for the TO-Mn/F/N-02 sample and chemical composition mapping is shown in Figure 1d–i. The EDX analysis results are evidencing the presence of Ti, O, Mn, F, and N and their homogeneous distribution across the bunch of nanotubes. The corresponding Mn to Ti atomic ratio can be determined as 0.016.

HRTEM imaging and SAED experiments confirmed the  $\text{TiO}_2(\text{B})$  structure in the examined samples. Figure 2a shows a bunch of nanotubes where different lattice spacings could be resolved. Most of them are in good agreement with theoretical ones for  $\text{TiO}_2(\text{B})$  and it is shown in more detail in Figure S2. The electron diffraction pattern for this area (Figure 2b) reveals a number of reflections which could be associated with the  $\text{TiO}_2(\text{B})$  phase. However, some observed spacings may also belong to the anatase phase (marked with \*). To clarify this point, we have found a well-oriented nanocrystal (Figure 2c). This nanocrystal's structure can be uniquely determined as a monoclinic  $\text{TiO}_2(\text{B})$  phase (PDF No. 46-1238) because it has a specific period  $d_{001} = 0.62$  nm. Figure 2d shows a Fourier transform of image Figure 2c.

For advanced phase analysis of the materials, the Ti  $L_{2,3}$  edges EELS spectra were studied, as shown in Figure S3 for the TO-Mn/F/N-04 sample as an example. The data clearly identify reflections of the bronze  $\text{TiO}_2$  phase [55] in the Ti edge EELS.

In order to evaluate the texture of the studied materials,  $\text{N}_2$  adsorption–desorption tests were carried out. It is established that the type IV isotherms with H3 hysteresis loops (Figure 3) are observed for all prepared products, indicating their porous structure.



**Figure 2.** (a) HRTEM-image of several TiO<sub>2</sub> nanotubes. (b) The electron diffraction pattern identifying bronze titania. (c) The magnified region of HRTEM-image shows the nanocrystal oriented in [−110] zone axis and (d) the corresponding Fast Fourier Transform image.

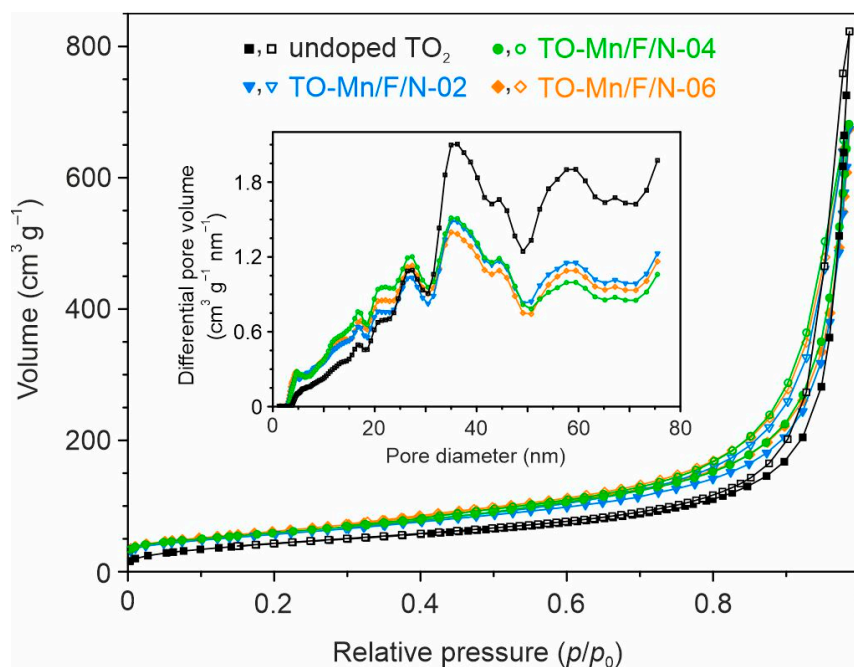


**Figure 3.** Nitrogen adsorption–desorption isotherms and pore size distribution curves (inset) for the undoped and Mn, F, N co-doped TiO<sub>2</sub> structures (the filled and open symbols represent, respectively, the adsorption and desorption data).

The pore size distribution curves (Figure 3, inset) show a wide range of pore sizes with maximums near 35–36 nm. From the NLDFT calculations, the total pore volume for

materials can be regarded as  $0.87\text{--}0.99\text{ cm}^3\text{ g}^{-1}$ , as listed in Table S1. The specific surface area estimation by NLDFT presents that (Mn, F, N)-doped samples exhibit larger values as compared to undoped ones (Table S1). Indeed, this parameter is  $145.6\text{ m}^2\text{ g}^{-1}$  for undoped  $\text{TiO}_2$ , whereas TO-Mn/F/N-02, TO-Mn/F/N-04, and TO-Mn/F/N-06 samples exhibited 197.7, 188.9, and  $203.0\text{ m}^2\text{ g}^{-1}$ , respectively. The observed phenomenon agrees with that from the literature [56,57] and suggests that dopants have an inhibiting effect on the growth of  $\text{TiO}_2$  crystallites. It should be pointed out that an increase in the concentration of dopants insignificantly influenced texture.

Next, XPS studies were performed to identify the chemical composition of (Mn, F, N)-doped  $\text{TiO}_2$  (TO-Mn/F/N-06 product). As can be seen in Figure 4a, there are distinguishable peaks for titanium, oxygen, manganese, and fluorine in the XPS survey spectrum. Besides, carbon in aliphatic and oxidized states was found on the material surface. These results agree with the EDX findings.

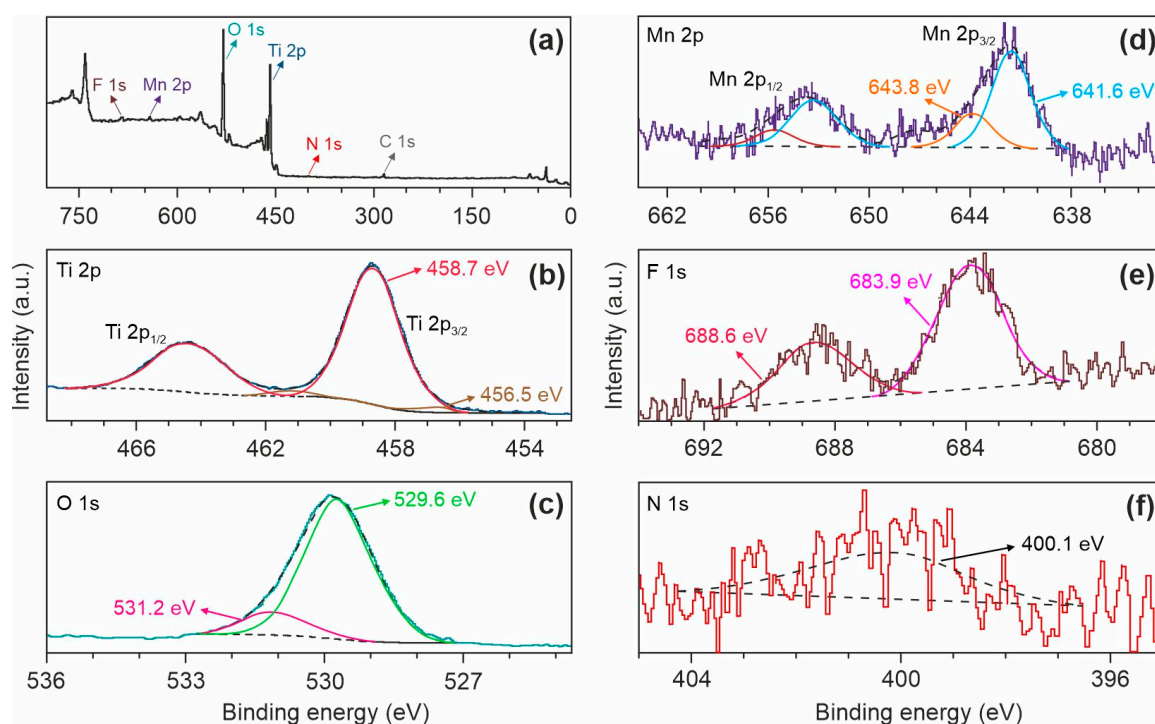


**Figure 4.** (a) XPS survey spectrum and corresponding high-resolution scans of the (b) Ti 2p, (c) O 1s, (d) Mn 2p, (e) F 1s, and (f) N 1s peaks for the TO-Mn/F/N-06 sample.

Figure 4b shows the Ti 2p core level that is split into a doublet of  $2p_{3/2}$  and  $2p_{1/2}$ . Two components were identified through deconvolution suggesting several different oxidation states of titanium: dominating  $\text{Ti}^{4+}$  at a binding energy ( $\text{Ti } 2p_{3/2}$ ) of 458.7 eV and  $\text{Ti}^{3+}$  situated at  $E_b(\text{Ti } 2p_{3/2}) = 456.5\text{ eV}$ . The existence of Ti with a valence of +3 in the TO-Mn/F/N-06 can be explained by an incorporation of  $\text{F}^-$  anions into the  $\text{TiO}_2$  oxygen sublattice during doping. The deconvolution of O 1s XPS spectrum (Figure 4c) shows the intensive peak centered at 529.6 eV due to  $\text{O}^{2-}$  in the  $\text{TiO}_2$  lattice and the contribution at a higher binding energy of 531.2 eV resulted from oxygen forming a double bond with carbon (i.e., amides, esters, and carboxyl moieties) [58,59]. The Mn 2p XPS spectrum (Figure 4d) is split due to spin-orbit coupling into a  $2p_{1/2}$ – $2p_{3/2}$  doublet. The computation reveals components with binding energies ( $\text{Mn } 2p_{3/2}$ ) of 641.6 eV (manganese in the +3 oxidation state [57]) and 643.8 eV (tetravalent manganese [60]). The F 1s line (Figure 4e) is divided into two peaks. The contribution at 683.9 eV is associated with fluorine anions adsorbed physically on the material surface, whereas the component at 688.6 eV indicates the substitution of  $\text{F}^-$  for  $\text{O}^{2-}$  in the  $\text{TiO}_2$  lattice due to which nonstoichiometric solid

solution is formed [61,62]. Treatment with a help of ammonium fluorides ( $\text{NH}_4\text{F}$ ,  $\text{NH}_4\text{HF}_2$ ) is a recognized route for materials fluorination. At the same time, as reported in [45],  $\text{NH}_4\text{F}$  or  $\text{NH}_4\text{HF}_2$  can serve as a source of nitrogen for preparing F and N co-doped titanium dioxide. The profound insight shows that nitrogen exists in the analyzed sample. Figure 4f demonstrates the N 1s XPS peak located at 400.1 eV. Based on the literature [63,64], it can be concluded that nitrogen occupies an interstitial position in the  $\text{TiO}_2$  crystal lattice forming  $\text{NO}_x$  species. Table S2 summarizes the positions and relative atomic percentages for the interpreted components.

In the XRD patterns of undoped and Mn, F, N co-doped  $\text{TiO}_2$  (Figure 5) a broadening of peaks is observed suggesting crystallites with nanoscopic dimensions. All considered samples contained two phases of titanium dioxide. Most of the reflections refer to the bronze titanium dioxide having a monoclinic structure with a  $C2/m$  space group (PDF No. 46-1238), whereas other ones belong to the anatase modification (PDF No. 73-1764).

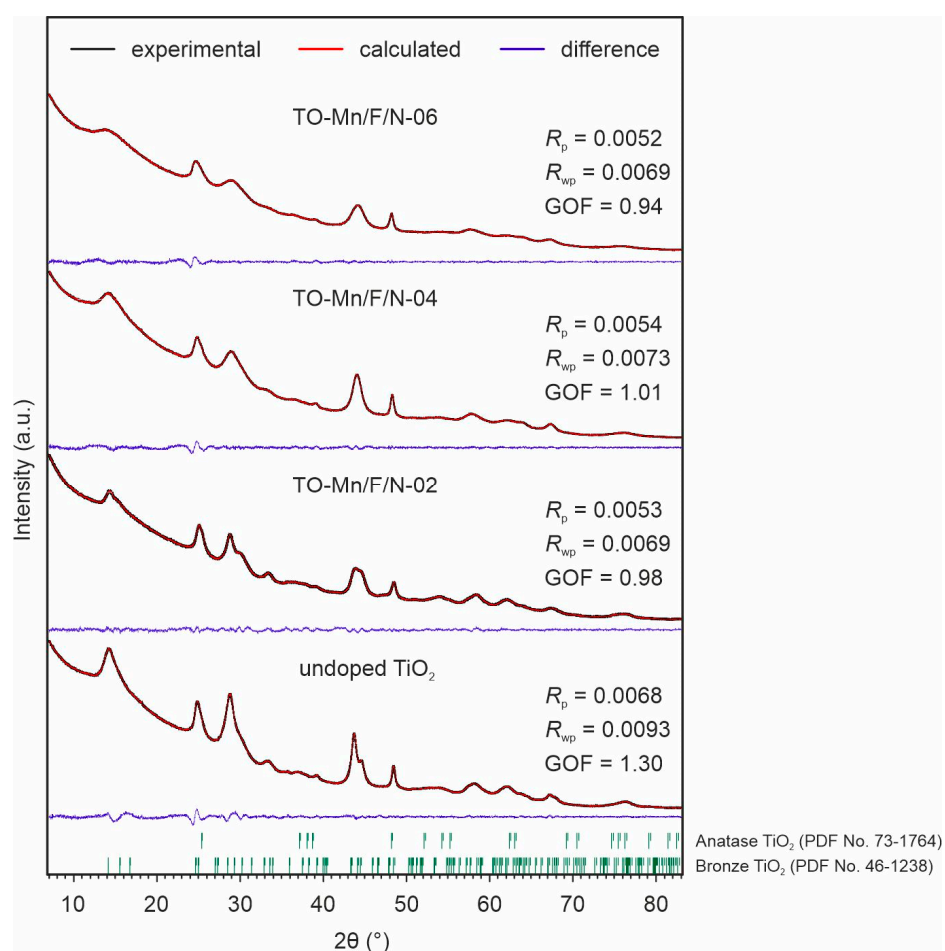


**Figure 5.** XRD patterns and Rietveld refinement results for the unmodified  $\text{TiO}_2$ , TO-Mn/F/N-02, TO-Mn/F/N-04, and TO-Mn/F/N-06 samples.

The bronze  $\text{TiO}_2$  is a metastable phase and under heat treatment can be easily converted to anatase [65]. The temperature of  $\text{TiO}_2(\text{B})$  to anatase phase transformation depends on several factors [66–69], including shape and dimensions of particles, and porosity, which are determined by the methodology of synthetic procedure (e.g., pressure, temperature, and process duration, pH of the medium, etc. in case of hydro- or solvothermal method). Herein, it was found that the synthesis of manganese-containing  $\text{TiO}_2$  in absence of ammonium hydrofluoride leads to the predominance of anatase in the composition of products (Figure S4). It is known that the phase transformations in titanium dioxide can be promoted/inhibited by the incorporation of impurities changing the diffusion mobility of ions

in the lattice. E.g., as reported in [70] doping with 1, 5, and 10 at.% manganese decreases the temperature of anatase to rutile transition by 50, 100, and 200 °C, respectively. Similar data are presented in [71–73] indicating the promotion effect of Mn on phase transition kinetics. The phase transformation is a result of a substitution of  $\text{Ti}^{4+}$  ions within the  $\text{TiO}_2(\text{B})$  lattice by Mn species with a smaller oxidation state, i.e.,  $\text{Mn}^{3+}$  ions, as found by XPS (Figure 4d). Indeed, in such a scenario, in order to maintain charge neutrality, the doubly positively charged oxygen vacancies (so-called  $F^{2+}$ -centers) would be formed in the crystal structure (Equation (1), hereinafter Kröger-Vink notation is used), allowing the  $\text{TiO}_2(\text{B})$  to anatase phase transition at lower temperatures.



here the defect equilibria are achieved because of doubly positively charged oxygen vacancy  $\text{V}_\text{O}^{\bullet\bullet}$  compensate two  $\text{Mn}'_{\text{Ti}}$  (Mn replacing Ti in its lattice site) defects with a single negative charge.

At the same time, as known doping the oxygen-deficient structures with fluorine frequently occurs through the annihilation of vacancies in the anionic sublattice (Equation (2)) [74]. The annihilation of such type of defects in the titanium dioxide is accompanied by changing the oxidation state of titanium (and/or manganese in our case) in the cation sublattice [75].



Besides the abovementioned, or in the case of elimination (completely “healing”) of oxygen vacancies, another outcome is possible: substitution of lattice  $\text{O}^{2-}$  ions by  $\text{F}^-$  species with a compensative (according to the electroneutrality principle) formation of  $\text{Ti}^{3+}$  defect states [74,75].

Concerning anatase both these mechanisms stabilize it, inhibiting transformation into rutile induced by the thermal treatment [75]. As seems, these effects may inhibit  $\text{TiO}_2(\text{B}) \rightarrow$  anatase phase transition in the case of Mn-, F-, and N-containing samples studied in this work.

Lastly, as it was found in [76], the modification of titanium dioxide by fluorine through a way that is not associated with its incorporation in the crystal lattice, namely if  $\text{F}^-$  ions are physically adsorbed at the surface, also influences thermal stability of anatase and dynamics of its transformation into rutile.

Riveted refinement data (Table S3) indicates the changes in lattice constants of both  $\text{TiO}_2(\text{B})$  and anatase phases when co-doped with (Mn, F, N). The calculated values of corresponding unit cell volumes demonstrate an increase of up to ~1.5% for modified samples as compared to the undoped ones. When in an octahedral environment, the ionic radius of  $\text{Mn}^{4+}$  (0.58 Å) is lesser than that of  $\text{Ti}^{4+}$  (0.605 Å). The radius of six-fold coordinated  $\text{Mn}^{3+}$  ion in the high-spin and low-spin states equals 0.645 or 0.58 Å, respectively. Because oxygen is a weak field ligand, the high-spin state can be predicted for trivalent manganese. The fluoride ion (1.3 Å) in a three-fold octahedral coordination geometry is smaller by 4.6% than the oxygen anion (1.36 Å). However, as mentioned above, fluorine incorporation into the  $\text{TiO}_2$  lattice results in the appearance of  $\text{Ti}^{3+}$  with an ionic radius of 0.67 Å (coordination number–6). The interstitial doping mechanism suggests a formation of  $\text{NO}_x$  or  $\text{NH}_x$  species at the interstitial sites within the  $\text{TiO}_2$  lattice [75,77], which could cause its expansion. As opposed to substitutional nitrogen-doping (replacement of  $\text{O}^{2-}$  by  $\text{N}^{3-}$  anions with a formation of vacancy-type defects in the oxygen sublattice), the interstitial type may be preferable in terms of stability of crystal framework due to slowing down of the temperature-induced dynamics of lattice and its evolution across the transition [75]. Thus, the observed distortions of  $\text{TiO}_2(\text{B})$  and anatase crystal lattices can be explained by a combination of factors, including the incorporation of  $\text{Mn}^{3+}/\text{Mn}^{4+}$  cations into the  $\text{Ti}^{4+}$  positions,  $\text{F}^-$  anions into the sites of oxygen vacancies or/and lattice  $\text{O}^{2-}$ , and nitrogen species into interstitials. On top of everything else, it should be pointed out that no other phases were detected in the XRD patterns of samples containing 2 at.% (TO-Mn/F/N-02) and 4 at.%

(TO-Mn/F/N-04) manganese, confirming the successful dissolution of  $\text{Mn}^{3+}/\text{Mn}^{4+}$  ions in the titanium dioxide structure with a formation of substitutional solid solutions. Traces of  $\text{MnO}_2$  were found in the TO-Mn/F/N-06 sample.

Figure 6a represents the UV-vis diffuse reflectance spectra of analyzed materials. It can be clearly seen that as compared to the undoped  $\text{TiO}_2$  the modified products absorb electromagnetic irradiation more intensively in both ultraviolet and visible regions. Besides, it is obvious that TO-Mn/F/N-02, TO-Mn/F/N-04, and TO-Mn/F/N-06 have an identical mechanism of optical activity. The improvement of light absorption properties correlates with a concentration of dopants. Furthermore, an analysis shows that (Mn, F, N) co-doping in titanium dioxide shifts the absorption edge to higher wavelengths (so-called redshift effect) indicating modification of the electronic band structure. Applying Kubelka–Munk theory (putting  $F(R_\infty)$  instead of  $\alpha$ ) to the Tauc relation (Equation (3)) for allowed indirect transitions ( $\gamma = 2$ ), the  $(F(R_\infty) \cdot hv)^{1/2}$  against  $hv$  dependences were further plotted (Figure 6b). The band gaps of analyzed products can be identified by points of intersection of the tangent lines and the horizontal axis, as shown in these graphs. Table S1 lists the band gaps of analyzed materials obtained by this technique. The  $E_g$  for undoped  $\text{TiO}_2$  has been estimated as 3.14 eV which is consistent with the literature data on bronze titanium dioxide [36,37]. At the same time, co-doping  $\text{TiO}_2$  decreases the band gap energy to 2.93, 2.69, and 2.18 eV with an increase in the Mn, F, and N content. It should be pointed out that doping degree has an influence on the color of products (inset in Figure 6b), which changes from white (undoped  $\text{TiO}_2$ ) to light grey (TO-Mn/F/N-02), grey (TO-Mn/F/N-04), and grey-brown (TO-Mn/F/N-06).

$$(\alpha \cdot hv)^{1/\gamma} = A(hv - E_g), \quad (3)$$

where  $\alpha$  is the absorption coefficient,  $hv$  is the photon's energy,  $F(R_\infty) = (1 - R_\infty)^2 / 2R_\infty$  is the Kubelka–Munk function,  $R_\infty$  is the reflectivity,  $A$  is the constant called the band tailing parameter.

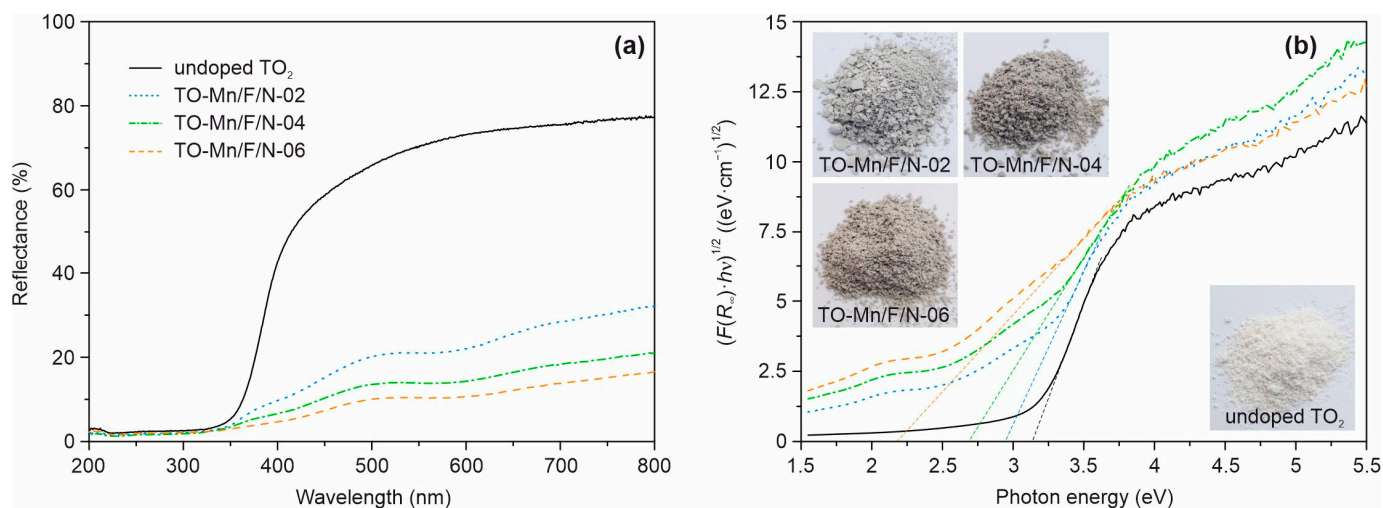


**Figure 6.** (a) UV-Vis diffuse reflectance spectra and (b) corresponding  $(F(R_\infty) \cdot hv)^{1/2}$  vs.  $hv$  plots of unmodified  $\text{TiO}_2$ , TO-Mn/F/N-02, TO-Mn/F/N-04, and TO-Mn/F/N-06 samples. The insets show photos of the analyzed powder products.

The observed effects can be explained by the appearing impurity and defect energy levels between valence and conduction bands of titanium dioxide. Indeed, manganese depending on the oxidation state can tend to generate localized electronic levels with different positions (energies) closer to the middle of the band gap [78]. In the diffuse reflectance spectra of (Mn, F, N)-containing materials absorption band in the region of 520–650 nm, becoming intense through doping, is assigned to  ${}^5T_{2g} \leftarrow {}^2E_g$  transition in  $\text{Mn}^{3+}$

ions with six-fold coordination [79,80]. The absorption band of  $\text{Mn}^{4+}$  in an octahedral environment (wavelengths up to 480 nm) lies within the region of the fundamental absorption of  $\text{TiO}_2$  [81]. The thorough observations allow us to distinguish the shoulder near 420 nm in analyzed UV-Vis spectra. For illustrative purposes, the registered diffuse reflectance spectra are represented as Kubelka–Munk function against wavelength plots, as displayed in Figure S5a. Doping with nitrogen is accompanied by the appearance of N 2p states above the valence band (O 2p): in the case of interstitial N—higher by 0.73 eV [63]. According to [82] in UV-Vis spectra of N-doped titanium dioxide the absorption bands at 400–550 nm are assigned to the nitrogen within the lattice. At the same time in analyzed  $\text{TiO}_2(\text{B})$ -based products this region corresponds also to the bands of  $\text{Mn}^{4+}$  ions. The 2p energy level of fluorine lies below O 2p (by 1.19 eV [83]), hence it has no response in the UV-Vis spectra. In contrast, as mentioned above, the incorporation of a fluorine atom into the crystal lattice of titanium dioxide donates one extra (with respect to lattice oxygen or  $\text{V}_\text{O}^{\bullet\bullet}$ ) electron, which is expected to localize in the 3d orbitals of the Ti atom forming  $\text{Ti}^{3+}$  defect states. The energy level related to  $\text{Ti}^{3+}$  is located at 0.82 eV below the conduction band [84], i.e., it lies within the band gap of  $\text{TiO}_2$ . To investigate the effect of fluorine and nitrogen on the electronic properties of analyzed materials, (F, N) co-doped titanium dioxide was synthesized and studied by UV-Vis spectroscopy (Figure S5b). As can be seen,  $E_g$  narrowed to 3.07 eV due to doping indicating F and/or N participation in tuning the electronic structure of (Mn, F, N) co-doped  $\text{TiO}_2(\text{B})$ . It should be noted that in overall the absorption profile of (F, N)-doped titanium dioxide (insert in Figure S5b) agrees with the literature ones for nitrogen-containing products [84,85]. The obtained results did not allow us to declare the predominance effect of nitrogen or fluorine on the electronic properties of studied (F, N) co-doped  $\text{TiO}_2(\text{B})$  and deeper insight is required in further work. Lastly, it should be mentioned that due to appearance of oxygen vacancies caused by charge compensation mechanisms in doped titanium dioxide ( $\text{TiO}_{2-\delta}$ ), as discussed ahead, the localized energy states at 0.75–1.18 eV below the conduction band [86,87] would be generated modifying electronic band structure.

To reveal and study the paramagnetic centers existing in the analyzed materials based on  $\text{TiO}_2(\text{B})$  the EPR investigations have been carried out. X-band EPR spectra of the TO-Mn/F/N-04 sample at 24,  $-80$  and  $-160$  °C are presented in Figure 7a. At room temperature, the spectra contain an intense resonance band with the value of  $g$ -factor  $\sim 2.00$ , which exhibits a feebly pronounced sextet structure, and two low-intensity resonances with the  $g$ -factors being equal to  $\sim 5.27$  and  $\sim 4.32$ . As the temperature decreases, the intensities of all EPR lines increase, while their characteristic features remain and become more pronounced. The component of the spectrum with  $g \sim 2.00$ , taking into account its sextet structure, can be assigned to paramagnetic manganese ions. As far as  $\text{Mn}^{3+}$  centers are not detected by the EPR method down to liquid helium temperatures due to the short spin-lattice relaxation times, it can be attributed to  $\text{Mn}^{2+}$  and/or  $\text{Mn}^{4+}$  ions. Moreover, the better resolution of the sextet structure in the Q-band (Figure S6a) indicates that it does not represent a superposition of resonances on these ions, but it is a resonance on one of them only. A clue to understanding the nature of the considered component of the spectrum is the average value of the peak-to-peak intervals of the sextet structure. The value of this parameter determined from the spectra measured in the Q-band (Figure S6a) is 8.96 mT. It is typical of the value of hyperfine structure constant of the EPR spectra of compounds containing  $\text{Mn}^{2+}$  ions in oxygen octahedra [88,89] and is noticeably larger than the average value of the same parameter for the EPR spectra of  $\text{Mn}^{4+}$  ions in the same crystal fields [89–92]. An acceptable approximation of the experimental Q-band EPR spectrum of the TO-Mn/F/N-04 sample at room temperature is possible by the sum of the spectrum with a sextet structure and the broad line with a Gaussian contour (Figure S6a). The second component of the spectrum can belong to manganese ions located in interstitial (non-lattice) positions. It can also belong to the “islands” of manganese oxide (MnO) on the surfaces and/or in the cavities of tubular  $\text{TiO}_2(\text{B})$  particles. The resonance with  $g \sim 4.32$  is characteristic of ions with  $3d^5$  configuration in crystal fields with a strong rhombic

component [93,94]. Therefore, a low-intensity resonance with this value of  $g$ -factor can result from both  $\text{Mn}^{2+}$  and  $\text{Fe}^{3+}$  ions. However, taking into account its width of  $\sim 8.5$  mT (Figure S6b), which is significantly below the expected value ( $\sim 45$  mT) for the sextet of  $\text{Mn}^{2+}$  ions, it should be considered as a resonance exactly on  $\text{Fe}^{3+}$  ions, which, apparently, enter the samples in trace amounts from their precursors. Note that it is also present in the spectrum of undoped  $\text{TiO}_2(\text{B})$  (Figure S6c). To comprehend the origin of another low-intensity resonance with  $g \sim 5.27$ , we have calculated the EPR spectra of the  $\text{Mn}^{4+}$  ion in a crystal field with strong rhombic distortion (Figure S6d), using the spin Hamiltonian parameters given in Table S4. The theoretical spectrum contains three sextets with  $g$ -factors being equal to 1.46, 2.00 and 5.46. For the low-field sextet the  $g$ -factor and width ( $\sim 55$  mT) are close to the values of the same parameters of the corresponding component of the experimental spectrum ( $\sim 52$  mT). Consequently, a small part of the manganese ions in the samples is in the +4 oxidation state. It is worth noticing that the EPR spectra of doped products do not contain resonances on electrons localized in oxygen vacancies, as well as resonances on  $\text{Ti}^{3+}$  ions. Taking into account the narrowing of the band gap due to co-doping (F, N) (Figure S5b), the above confirms the effect of nitrogen impurity on the electronic properties of  $\text{TiO}_2(\text{B})$ .

The enhancement in conductive properties due to doping is confirmed by impedance measurements illustrated in Figure 7b.

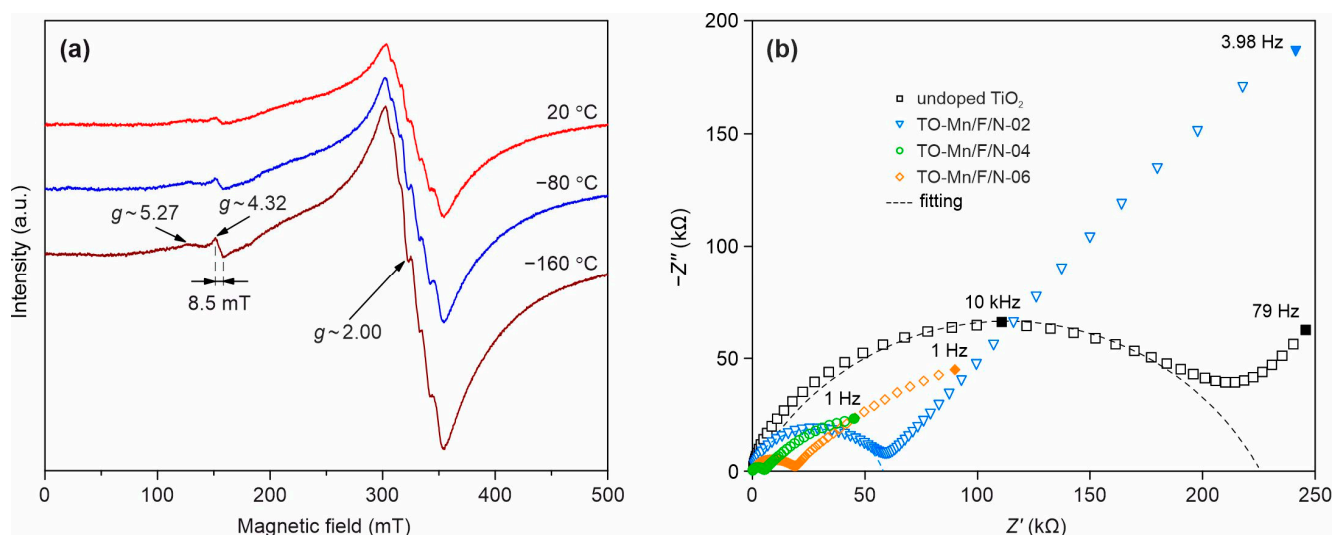


**Figure 7.** (a) X-band EPR spectra of (Mn, F, N) co-doped  $\text{TiO}_2(\text{B})$  at different temperatures and (b) Impedance spectra of undoped  $\text{TiO}_2$ , TO-Mn/F/N-02, TO-Mn/F/N-04, and TO-Mn/F/N-06 samples with corresponding fitting curves.

The registered spectra represented as Nyquist plots have a typical form: a semicircle located in the high-frequency region of the spectrum (from 0.8 kHz–4 MHz to 8 kHz–5 MHz) and a straight line in the rest of the low-frequency range that does not intersect the real impedance axis. Such spectra as a whole demonstrate both the presence of kinetic control and a diffusion-controlled region. The bulk resistance was calculated in a certain frequency range of each sample impedance spectrum (zoom-in view of spectra is shown in Figure S7; calculated EIS parameters are summarized in Table S5) using the EEC displayed in the inset of Figure S7. The applied EEC involves the following elements:  $R_{el}$  including the resistance of lead wires—assuming that both contacts are of identical nature (may include capacitance, inductance)—and appearing when analyzing the impedance of low-resistance materials;  $R_b$  and  $C_g$  corresponding to the resistance and geometric capacitance of the sample;  $R_{ct}$  and  $C_{dl}$  associating with the resistance to charge transfer and capacitance of the electrical double layer, which represent the processes occurring at the electrode/sample interface and related with the redistribution of charge near the interface. The calculated values of conductivity

for unmodified  $\text{TiO}_2$ , TO-Mn/F/N-02, TO-Mn/F/N-04, and TO-Mn/F/N-06 samples were as follows:  $2.9 \times 10^{-7}$ ,  $2.3 \times 10^{-6}$ ,  $5.7 \times 10^{-6}$ , and  $4.0 \times 10^{-6} \text{ S cm}^{-1}$  (Table S1) Hence, in general, there is a clear tendency for the samples to increase the conductive properties due to doping. As can be seen from the data, the maximum decrease in resistance was recorded for TO-Mn/F/N-04 material that has a conductivity of more than 40 times higher in comparison with undoped  $\text{TiO}_2$ .

Figure 8a depicts charge/discharge profiles of the first cycle at a current density of  $70 \text{ mA g}^{-1}$  for unmodified and (Mn, F, N) co-doped  $\text{TiO}_2$  samples in the half-cell configuration.

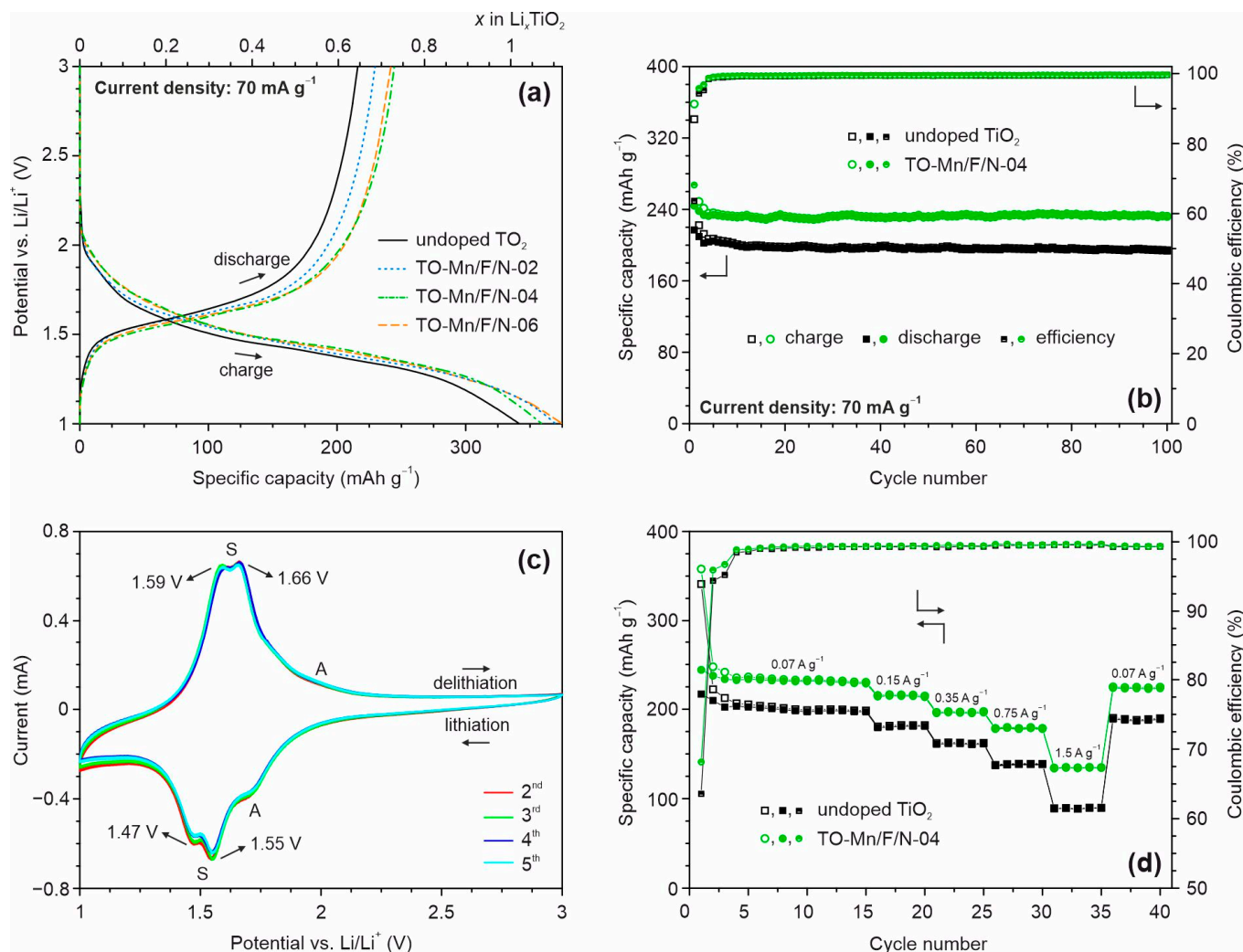


**Figure 8.** (a) Charge/discharge profiles of the first cycle and (b) subsequent cycling at  $70 \text{ mA g}^{-1}$  for undoped  $\text{TiO}_2$  and TO-Mn/F/N-04 material, (c) CV curves for TO-Mn/F/N-02 electrode at a scan rate of  $0.1 \text{ mV s}^{-1}$ , (d) rate capability at different current densities of unmodified and (Mn, F, N) co-doped  $\text{TiO}_2$  (TO-Mn/F/N-04 sample) in the half-cell configuration.

As can be seen, the curves contain voltage regions with a slope during charging and discharging at the potentials of approximately 1.5 and 1.6 V, respectively, which is typical for  $\text{TiO}_2(\text{B})$ , lithiation and delithiation which can be expressed as follows:



where  $n$  is the number of electrons transferred in the redox process ( $n = 1.01$  for nanocrystalline  $\text{TiO}_2(\text{B})$  [80]).

Upon initial charge (lithiation of  $\text{TiO}_2$ ) the electrodes yield the following specific capacities:  $341 \text{ mAh g}^{-1}$  (undoped product),  $369 \text{ mAh g}^{-1}$  (TO-Mn/F/N-02),  $358 \text{ mAh g}^{-1}$  (TO-Mn/F/N-04), and  $374 \text{ mAh g}^{-1}$  (TO-Mn/F/N-06). The obtained values exceed the theoretical capacity of titanium dioxide ( $335 \text{ mAh g}^{-1}$ ). This phenomenon has been repeatedly noted in the literature for LIBs anodes based on  $\text{TiO}_2$  nanomaterials having a large specific surface area. As reported in [95,96], this is due to decomposition reactions of lithium-ion battery electrolyte (at the potentials near 1 V [97,98]) resulting in the formation of a solid electrolyte interphase layer at the electrode surface. The first cycle discharge (delithiation) capacity for undoped  $\text{TiO}_2$  is equal to  $217 \text{ mAh g}^{-1}$  corresponding to the extraction of about 0.65 lithium ion per formula unit. The TO-Mn/F/N-02, TO-Mn/F/N-04, and TO-Mn/F/N-06 electrodes during initial discharge deliver a capacity of  $228 \text{ mAh g}^{-1}$  (extraction of around  $0.68 \text{ Li}^+$ ),  $244 \text{ mAh g}^{-1}$  ( $0.73 \text{ Li}^+$ ), and  $237 \text{ mAh g}^{-1}$  ( $0.71 \text{ Li}^+$ ), respectively. Among the studied materials, TO-Mn/F/N-04 shows the best efficiency during the first cycle of approximately 68.2%. It should be noted that for modified materials the smaller hysteresis (voltage gap) between charge and discharge voltage profiles is detected. This indicates an improved carrier transport properties due to high specific surface area and porosity, changes in the crystal and electronic structure. Figure 8b shows the varying of capacity during the subsequent cycling for undoped titanium dioxide and (Mn, F, N) co-doped  $\text{TiO}_2$  (TO-Mn/F/N-04 sample). The data represent that (Mn, F, N)-containing  $\text{TiO}_2$  maintains a capacity of  $231.5 \text{ mAh g}^{-1}$  after 100 charge/discharge cycles with a Coulombic efficiency of 99.6%. This corresponds to the capacity retention of almost 95%. By the way, the major capacity loss occurs during the initial 5–7 cycles. The drop in capacity is calculated as  $0.009 \text{ mAh g}^{-1}$  per cycle between 7 and 100 cycles for the TO-Mn/F/N-04 electrode. The unmodified titanium dioxide realizes the capacity of  $194 \text{ mAh g}^{-1}$  after 100 cycles with the retention of about 90%. The obtained data indicate that doping enhances the lithium insertion/extraction ability of  $\text{TiO}_2(\text{B})$ . The cycling performance for TO-Mn/F/N-02 and TO-Mn/F/N-06 electrodes is illustrated in Figure S8a.

Cyclic voltammetry studies in the half-cell assembly were carried out to visualize the mechanism of reduction/oxidation of  $\text{TiO}_2$  co-doped with manganese, fluorine, and nitrogen. CV curves registered between the 2nd and the 5th cycles at a scan rate of  $0.1 \text{ mV s}^{-1}$  for the TO-Mn/F/N-02 are represented in Figure 8c. The voltammograms exhibited peaks near 1.47 and 1.55 V at the cathodic region and around 1.59 and 1.66 V at the anodic branch. These maxima (so-called S-peaks) are characteristic of the lithiation/delithiation of bronze  $\text{TiO}_2$  [26]. Remarkably, S-peaks possess a high symmetry and starting from the 4th cycle almost overlap with each other representing that this electrochemical reaction is highly reversible. Slight irreversible losses which occur within 2nd and 3rd cycles can be associated with lithium trapped in the material (not extracted) and/or continuing formation (evolution) of the solid electrolyte interphase layer. Besides S-peaks, it is observed a cathodic maximum at around 1.7 V and a weak shoulder in the anodic region near 2 V in the CV curves. These peaks correspond to the reduction/oxidation of anatase (A-peaks) [99]. Besides S-peaks, a cathodic maximum at around 1.7 V and a weak shoulder in the anodic region near 2 V are observed in CV curves which correspond to the reduction/oxidation of anatase (A-peaks). No other redox peaks were observed in the CVs indicating that except  $\text{Ti}^{4+}/\text{Ti}^{3+}$  no other redox couple is involved.

The rate capability of unmodified and (Mn, F, N) co-doped  $\text{TiO}_2$  materials were tested in the half-cell configuration by charge/discharge at various current loads of 150, 350, 750, and  $1500 \text{ mA g}^{-1}$  for every five cycles (Figures 8d and S7a). Before these tests, the activation at  $70 \text{ mA g}^{-1}$  for the initial fifteen cycles was performed. As observed, doping improves the rate performance of bronze titanium dioxide. Indeed, the reversible capacities of about 214, 196, 178, and  $134 \text{ mAh g}^{-1}$  were obtained at 150, 350, 750, and  $1500 \text{ mA g}^{-1}$ , respectively, for the TO-Mn/F/N-04 electrode. Whereas, undoped  $\text{TiO}_2$  delivered the capacities of 180, 161, 138, and  $89 \text{ mAh g}^{-1}$  at the same current densities. Notably, no obvious capacity loss is detected for samples when a current load was returned to  $70 \text{ mA g}^{-1}$  after the rate experiments due to the favorable features of the tubular nanostructures. The difference

in rate capability of analyzed electrodes can be revealed obviously from the capacity retention against the applied current density plot (Figure S8b). As viewed from these data, the capacity retention of TO-Mn/F/N-04 material is about 57.5% for the discharge between 70 and 1500 mA g<sup>-1</sup>, while it is only 44.3% for unmodified TiO<sub>2</sub>. Thus, doping increases the tolerance of TiO<sub>2</sub>(B) to current loads. As seems it could be due to enhanced conductive properties of doped TiO<sub>2</sub>(B). Table S6 represents the electrochemical parameters of previously reported LIBs anodes based on doped bronze TiO<sub>2</sub> as compared to that for (Mn, F, N)-containing TiO<sub>2</sub>(B) [38–48]. The results show that nanotubular (Mn, F, N) co-doped TiO<sub>2</sub>(B) is not inferior to others of the same type.

In order to understand the mechanism of improved electrochemical performances of the co-doped TiO<sub>2</sub>(B) nanotubes, EIS experiments were carried out in the half-cell configuration for electrodes based on undoped TiO<sub>2</sub> and TO-Mn/F/N-04 sample, as shown in Figure 9. The spectra were collected at the potential of 3 V of the first charge (prior cycling). As can be seen from obtained data, the impedance spectra in Nyquist coordinates of both electrodes show depressed paired semicircles at the high and middle frequencies representing information about the solid electrolyte interphase layer and charge transfer process. The low-frequency region of spectra is represented by an arc with a slope exceeding 45°, which characterizes the diffusion-controlled process. The spectra were fitted using an equivalent electrical circuit (inset of Figure 9) composed of the ohmic resistance of cell ( $R_s$ ), ionic resistance ( $R_f$ ) and geometrical capacitance ( $C_f$ ) of the SEI film, charge-transfer resistance ( $R_{ct}$ ) and double layer capacitance ( $C_{dl}$ ), Warburg impedance ( $Z_W$ ) associated with the diffusion of lithium ions. The results of fitting are presented in Table S7. The data indicate that in comparison with TO-Mn/F/N-04 electrode undoped TiO<sub>2</sub> has higher  $R_s$  and  $R_{ct}$  due to the poorer conductivity and the smaller  $R_f$  because of lower specific surface area. To understand the effects of TiO<sub>2</sub>(B) doping on Li<sup>+</sup> diffusion kinetics, the low-frequency region of spectra was next analyzed. To determine the lithium diffusion coefficients ( $D_{Li}$ ) for studied samples the following equation was used:

$$D_{Li} = R^2 T^2 / 2 S^2 n^2 F^4 C_{Li}^2 \sigma_W^2 \quad (5)$$

where  $R$  is the gas constant (8.31 J K<sup>-1</sup> mol<sup>-1</sup>);  $S$  is the electrode surface area (0.50 cm<sup>2</sup>);  $T$  is the absolute temperature (298.15 K);  $F$  is the Faraday constant (96,485.33 C mol<sup>-1</sup>);  $C_{Li}$  is the concentration of lithium in the TiO<sub>2</sub>(B) (1.39·10<sup>-3</sup> mol cm<sup>-3</sup>);  $\sigma_W$  is the Warburg factor ( $\sigma_W = dZ'/d\omega^{-1/2}$ ), which can be estimated from the slope of the linear fitting of  $Z'$  vs.  $\omega^{-1/2}$  plots (inset of Figure 9).

The calculated lithium diffusion coefficients were  $1.0 \times 10^{-11}$  and  $2.1 \times 10^{-11}$  cm<sup>2</sup> s<sup>-1</sup> for undoped TiO<sub>2</sub> and TO-Mn/F/N-04 electrodes, respectively, which are close to the values reported by other authors [40,100]. It is seen that doping is accompanied by facilitating and fastening the charge carriers' diffusion, probably, due to structural changes in TiO<sub>2</sub>(B) lattice. The observed effects can serve as another reason for the improved electrochemical behavior of doped samples.

Because of TiO<sub>2</sub>-based materials owing capability to use for both high-rate and low-temperature LIBs the performance of Mn, F, N co-doped TiO<sub>2</sub>(B) was studied at -15 and -20 °C using the 1 M solution of LiClO<sub>4</sub> in the mixture of propylene carbonate and 1,2-dimethoxyethane (84:16, vol. ratio) as electrolyte. The measurements were carried out at the current rate of 70 mA g<sup>-1</sup> after the pre-cycling at room temperature. Figure 10 represents the charge/discharge profiles registered at different temperature conditions.

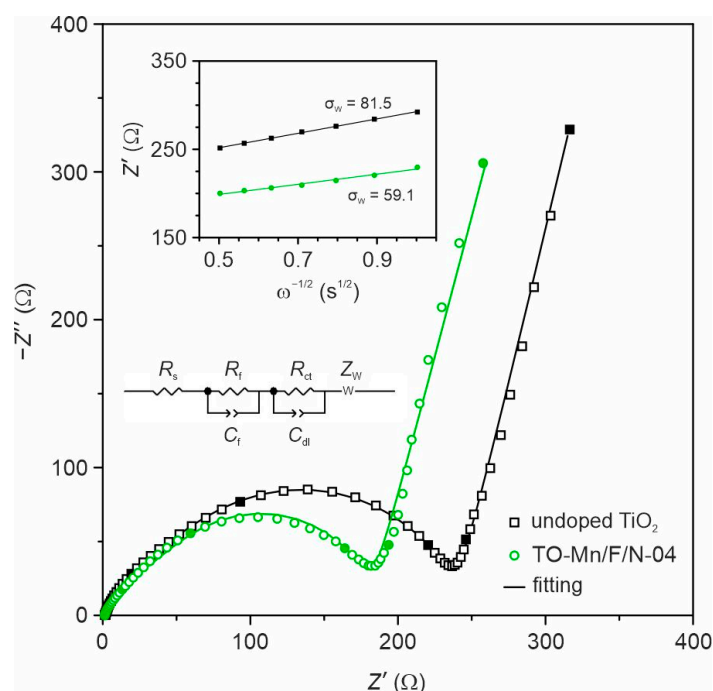


**Figure 9.** EIS spectra for undoped  $\text{TiO}_2$  and TO-Mn/F/N-04 electrodes in the half-cells registered at 3 V (frequencies of 0.1, 1, 10, 100, and 1000 Hz are marked with filled symbols). The insets show EEC applied for fitting and plots of real impedance against the inverse square root of the angular frequency used for estimation of the Warburg factor.

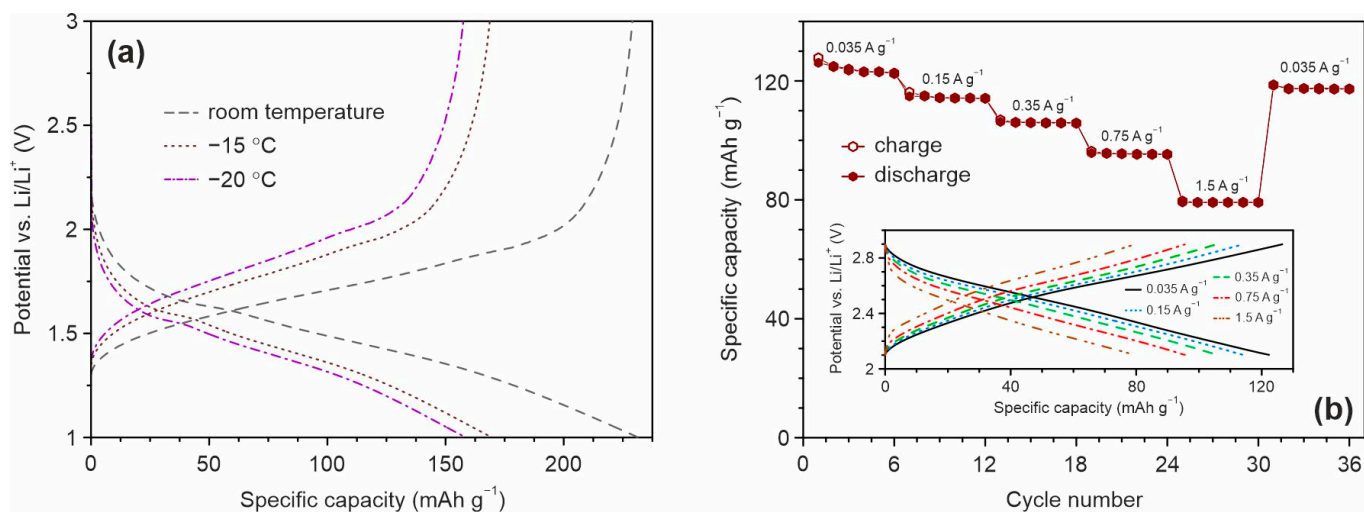


**Figure 10.** (a) Charge and discharge profiles for TO-Mn/F/N-04 electrode at room temperature,  $-15$  and  $-20$  °C registered at a current density of  $70 \text{ mA g}^{-1}$  in the half-cell configuration and (b) rate capability studies (after pre-cycling CV experiments) of the  $\text{TiO}_2(\text{B})/\text{LiMn}_2\text{O}_4$  full-cell in the range of 2.1 and 2.9 V at various current densities with the corresponding charge/discharge profiles (inset).

The results demonstrate that the material could deliver a reversible capacity of around 169 and  $158 \text{ mAh g}^{-1}$  at  $-15$  and  $-20$  °C, respectively, resulting in a retention of about 74 and 69% in comparison with that at room temperature ( $229 \text{ mAh g}^{-1}$ ). Thus, these experiments reveal the remarkable steadiness of Mn, F, and N co-doped  $\text{TiO}_2(\text{B})$  nanotubes, even when used under extreme specifications, and additionally demonstrate their feasibility for practical lithium-ion storage.

To further evaluate the practicalities of Mn, F, and N co-doped  $\text{TiO}_2(\text{B})$  nanotubes, full-cell experiments with the  $\text{LiMn}_2\text{O}_4$  cathode between 2.1 and 2.9 V were performed.

Figure 10b illustrates the variation of the specific capacity of  $\text{TiO}_2(\text{B})/\text{LiMn}_2\text{O}_4$  at different current loads registered after pre-cycling CV tests. It is obvious to note that the rate performance of nanotubular (Mn, F, N)-doped  $\text{TiO}_2(\text{B})$  in the full-cell configuration is attractive. The reversible capacity of about 123, 114, 106, 95, and 79  $\text{mAh g}^{-1}$  was obtained when the current density increased in the range from 35 to 150, 350, 750, and 1500  $\text{mA g}^{-1}$ . The corresponding charge/discharge profiles for  $\text{TiO}_2(\text{B})/\text{LiMn}_2\text{O}_4$  cell is shown in the inset in Figure 10b. Importantly, after the high-current charge/discharge cycling capacity of the full cell is returned to 117  $\text{mA g}^{-1}$  indicating the noteworthy recovery ability. It should be noted that  $\text{LiMn}_2\text{O}_4$  due to an operating voltage of around 4 V vs.  $\text{Li}/\text{Li}^+$  is not the proper cathode to test the performance of  $\text{TiO}_2$ -based anodes. To make good use of the  $\text{TiO}_2(\text{B})$ ,  $\text{LiMn}_{1.5}\text{Ni}_{0.5}\text{O}_4$  operating at a potential of 4.7 V vs.  $\text{Li}/\text{Li}^+$  or  $\text{LiFePO}_4$  having a capacity of 160–170  $\text{mAh g}^{-1}$  are recommended to apply [101,102].

#### 4. Conclusions

In summary, a Mn, F, and N co-doping strategy has been developed to enhance the electrochemical performance of  $\text{TiO}_2(\text{B})$  nanotubes for lithium storage. The doping of  $\text{TiO}_2(\text{B})$  was realized via one-step hydrothermal synthesis. The obtained  $\text{TiO}_2(\text{B})$  has a nanotubular morphology and possesses high porosity (total volume of around  $1 \text{ cm}^3 \text{ g}^{-1}$ ) and a large specific surface area (about  $200 \text{ m}^2 \text{ g}^{-1}$ ). It is found that doping with manganese decreases the temperature of  $\text{TiO}_2(\text{B})$  to the anatase phase transition. The importance of co-doping with fluorine is explained by the stabilization of bronze titanium dioxide. The incorporation of dopants causes the crystallographic changes in  $\text{TiO}_2(\text{B})$  accompanied by the increase of its unit cell volume. Through Mn and N co-doping the electronic structure of  $\text{TiO}_2(\text{B})$  is modified and band gap energy reduces from 3.14 to 2.18 eV. This results in an increase of  $\text{TiO}_2(\text{B})$  electronic conductivity by one order of magnitude. Doping of  $\text{TiO}_2(\text{B})$  gives rise to a chemical diffusion coefficient (about two times) facilitating and fastening the Li-ion diffusivity. The synergistic effect of Mn, F, and N doping improves the electrochemical properties of  $\text{TiO}_2(\text{B})$  nanotubes in lithium-ion batteries. In the half-cell configuration, the specific capacity is equal to 231.5  $\text{mAh g}^{-1}$  after 100 charge/discharge cycles at 70  $\text{mA g}^{-1}$  and 134  $\text{mAh g}^{-1}$  can be retained at a current density of 1500  $\text{mA g}^{-1}$ . Combining (Mn, F, N) co-doped  $\text{TiO}_2(\text{B})$  with  $\text{LiMn}_2\text{O}_4$  in the full-cell configuration a capacity of 123, 114, 106, 95, and 79  $\text{mAh g}^{-1}$  was realized at 35, 150, 350, 750, and 1500  $\text{mA g}^{-1}$  with the average operating voltage of  $\sim 2.5$  V. The (Mn, F, N)-containing  $\text{TiO}_2(\text{B})$  demonstrates a good low-temperature lithium storage performance with a capacity retention of 70% at  $-20$  °C. This study provides new insight into the doping strategy of  $\text{TiO}_2(\text{B})$ . The results demonstrate that (Mn, F, N) co-doping is an effective approach to tune the conductivity, structure, and texture of  $\text{TiO}_2(\text{B})$  nanomaterials as well as to control phase purity in order to design advanced lithium-ion batteries based on high-performance and environmentally benign materials. Furthermore, this doping strategy can also be applied for applications beyond batteries to develop next-generation devices (photocatalysts, sensors, solar cells, magnetics, etc.) based on such materials in the near future.

**Supplementary Materials:** The following supporting information can be downloaded at: <https://www.mdpi.com/article/10.3390/batteries9040229/s1>, Figure S1: SEM-micrographs for the undoped  $\text{TiO}_2$ , TO-Mn/F/N-02 and TO-Mn/F/N-06 products; Figure S2: (a) Crystallographic orientation of  $\text{TiO}_2(\text{B})$  crystals determined by HRTEM imaging in the TO-Mn/F/N-04 sample and (b) corresponding Fast Fourier Transform pattern; Figure S3: Experimental EELS spectra of Ti  $L_{2,3}$ -edges for the for the TO-Mn/F/N-04 sample and the commercial anatase  $\text{TiO}_2$  examined for comparison; Figure S4: XRD pattern of product doped with 4 at.% Mn, synthesized without  $\text{NH}_4\text{HF}_2$  (Bruker D8Advance diffractometer,  $\text{CuK}\alpha$ -radiation); Figure S5: (a) UV-vis diffuse reflectance spectra represented as Kubelka-Munk function against wavelength plots for the undoped  $\text{TiO}_2$ , TO-Mn/F/N-02, TO-Mn/F/N-04, and TO-Mn/F/N-06 products and (b) Tauc plot for the (F, N) co-doped  $\text{TiO}_2$  with the corresponding UV-vis absorption curve (inset); Figure S6: (a) Approximation (1) of the experimental Q-band EPR spectrum of the TO-Mn/F/N-04 sample at room temperature (2) by the sum of the spectrum with a sextet structure (3) and a single line with a Gaussian contour (4), (b) low field

region of the X-band EPR spectrum at  $-160\text{ }^{\circ}\text{C}$ , (c) the X-band EPR spectrum of undoped titanium dioxide, (d) simulated X-band EPR spectra of  $\text{Mn}^{4+}$  ions in the crystal fields with strong rhombic distortion; spectra "a" and "b" differ in the width ( $\Delta B$ ) of the hyperfine structure lines (see Table S4); Figure S7: Zoom-in impedance spectra of the undoped  $\text{TiO}_2$ , TO-Mn/F/N-02, TO-Mn/F/N-04, and TO-Mn/F/N-06 materials and the EEC (inset) used for fitting; Figure S8: (a) Evolution of capacity during cycling under various current loads for TO-Mn/F/N-02 and TO-Mn/F/N-06 electrodes, (b) capacity retention at various current densities as compared to that at  $70\text{ mA g}^{-1}$  for undoped  $\text{TiO}_2$ , TO-Mn/F/N-02, TO-Mn/F/N-04, and TO-Mn/F/N-06 materials; Table S1: Specific surface area, total pore volume, band gap energy, and conductivity of  $\text{TiO}_2$  samples co-doped with Mn, F, N as compared to unmodified one; Table S2: Quantification results obtained by XPS analysis for TO-Mn/F/N-06 sample; Table S3: The Rietveld refinement results for structures existed in unmodified and (Mn, F, N) co-doped  $\text{TiO}_2$  samples; Table S4: Spin-Hamiltonian parameters used to simulate the EPR spectra of  $\text{Mn}^{4+}$  ions in crystal fields with strong rhombic distortion; Table S5: Calculated EIS parameters for unmodified and (Mn, F, N) co-doped  $\text{TiO}_2$  samples; Table S6: Electrochemical performance of the doped  $\text{TiO}_2(\text{B})$  anodes in lithium-ion batteries; Table S7: The fitting results for EIS spectra of electrodes based on undoped  $\text{TiO}_2$  and TO-Mn/F/N-04 sample and the calculated lithium diffusion coefficient values.

**Author Contributions:** Conceptualization, D.P.O., S.L.S. and S.V.G.; data curation, D.P.O., S.L.S. and S.V.G.; formal analysis, D.P.O., E.B.M., A.A.S., A.B.P., A.M.Z., A.Y.U. and V.Y.M.; funding acquisition, D.P.O.; investigation, D.P.O., A.A.S., E.B.M., A.B.P., A.M.Z., A.Y.U. and V.Y.M.; methodology, D.P.O., E.B.M., A.A.S., A.B.P., A.M.Z. and A.Y.U.; project administration, D.P.O., S.L.S. and S.V.G.; resources, D.P.O., A.A.S. and S.V.G.; supervision, S.V.G.; validation, D.P.O., A.A.S., S.L.S. and S.V.G.; visualization, D.P.O., E.B.M., A.B.P., A.Y.U., V.Y.M. and A.M.Z.; writing—original draft preparation, D.P.O., E.B.M., A.B.P., A.Y.U., S.L.S. and S.V.G.; writing—review and editing, D.P.O., A.B.P., A.M.Z., S.L.S. and S.V.G. All authors have read and agreed to the published version of the manuscript.

**Funding:** Financial support from the Russian Science Foundation (grant No. 19-73-10017) is gratefully acknowledged.

**Data Availability Statement:** The data presented in this study are available on request from the corresponding author.

**Acknowledgments:** X-ray diffraction studies were carried out in the Core Faculty "Far East Center of Structural Investigations" at the Institute of Chemistry of Far Eastern Branch of the Russian Academy of Sciences (Vladivostok, Russia) with budgetary financing (theme No. FWFN-2022-0004). The authors are grateful to colleagues, namely Valery G. Kuryavyi (collection of SEM data), Denis A. Saritsky (EPR spectra analysis), and A.V. Gerasimenko (Rietveld refinement).

**Conflicts of Interest:** The authors declare no conflict of interest.

## References

1. Zhao, J.; Liu, K.; Lin, X. Toxic Effects of the Interaction of Titanium Dioxide Nanoparticles with Chemicals or Physical Factors. *Int. J. Nanomed.* **2013**, *8*, 2509–2520. [[CrossRef](#)] [[PubMed](#)]
2. Shejale, K.P.; Krishnapriya, R.; Patil, H.; Laishram, D.; Rawal, P.; Sharma, R.K. Recent Advances in Ultra-Low Temperature (Sub-Zero to  $100\text{ }^{\circ}\text{C}$ ) Synthesis, Mechanism and Applications of Titania ( $\text{TiO}_2$ ) Nanoparticles. *Mater. Adv.* **2021**, *2*, 7502–7529. [[CrossRef](#)]
3. Jacobs, J.F.; van de Poel, I.; Osseweijer, P. Sunscreens with Titanium Dioxide ( $\text{TiO}_2$ ) Nano-Particles: A Societal Experiment. *Nanoethics* **2010**, *4*, 103–113. [[CrossRef](#)] [[PubMed](#)]
4. Morsella, M.; D'Alessandro, N.; Lanterna, A.E.; Scaiano, J.C. Improving the Sunscreen Properties of  $\text{TiO}_2$  through an Understanding of Its Catalytic Properties. *ACS Omega* **2016**, *1*, 464–469. [[CrossRef](#)] [[PubMed](#)]
5. Fujishima, A.; Honda, K. Electrochemical Photolysis of Water at a Semiconductor Electrode. *Nature* **1972**, *238*, 37–38. [[CrossRef](#)]
6. Yan, H.; Zhang, D.; Qilu, Duo, X.; Sheng, X. A Review of Spinel Lithium Titanate ( $\text{Li}_4\text{Ti}_5\text{O}_{12}$ ) as Electrode Material for Advanced Energy Storage Devices. *Ceram. Int.* **2021**, *47*, 5870–5895. [[CrossRef](#)]
7. Mele, G.; Del Sole, R.; Lü, X. Applications of  $\text{TiO}_2$  in Sensor Devices. In *Titanium Dioxide ( $\text{TiO}_2$ ) and Its Applications*; Elsevier: Amsterdam, The Netherlands, 2021; pp. 527–581.
8. Bai, J.; Zhou, B. Titanium Dioxide Nanomaterials for Sensor Applications. *Chem. Rev.* **2014**, *114*, 10131–10176. [[CrossRef](#)]
9. Yin, Z.F.; Wu, L.; Yang, H.G.; Su, Y.H. Recent Progress in Biomedical Applications of Titanium Dioxide. *Phys. Chem. Chem. Phys.* **2013**, *15*, 4844. [[CrossRef](#)]

10. Jafari, S.; Mahyad, B.; Hashemzadeh, H.; Janfaza, S.; Gholikhani, T.; Tayebi, L. Biomedical Applications of TiO<sub>2</sub> Nanostructures: Recent Advances. *Int. J. Nanomed.* **2020**, *15*, 3447–3470. [[CrossRef](#)]
11. Adachi, T.; Latthe, S.S.; Gosavi, S.W.; Roy, N.; Suzuki, N.; Ikari, H.; Kato, K.; Katsumata, K.; Nakata, K.; Furudate, M.; et al. Photocatalytic, Superhydrophilic, Self-Cleaning TiO<sub>2</sub> Coating on Cheap, Light-Weight, Flexible Polycarbonate Substrates. *Appl. Surf. Sci.* **2018**, *458*, 917–923. [[CrossRef](#)]
12. Kameya, Y.; Yabe, H. Optical and Superhydrophilic Characteristics of TiO<sub>2</sub> Coating with Subwavelength Surface Structure Consisting of Spherical Nanoparticle Aggregates. *Coatings* **2019**, *9*, 547. [[CrossRef](#)]
13. Kim, S.K.; Kim, K.M.; Jeong, D.S.; Jeon, W.; Yoon, K.J.; Hwang, C.S. Titanium Dioxide Thin Films for Next-Generation Memory Devices. *J. Mater. Res.* **2013**, *28*, 313–325. [[CrossRef](#)]
14. Kim, B.; Kang, T.; Song, S.; Jung, C.; Lee, J.; Cheon, S.; Jeon, H. The Effect of O<sub>2</sub> Plasma Post-Treatment on Atomic Layer Deposited TiO<sub>2</sub> Thin Films. *Vacuum* **2022**, *199*, 110957. [[CrossRef](#)]
15. Nematov, D.D.; Khusenzoda, M.A.; Burhonzoda, A.S.; Kholmurodov, K.T.; Lyubchik, A.; Ibrahim, M. Investigation of Structural and Optoelectronic Properties of N-Doped Hexagonal Phases of TiO<sub>2</sub> (TiO<sub>2-x</sub>N<sub>x</sub>) Nanoparticles with DFT Realization: Optimization of the Band Gap and Optical Properties for Visible-Light Absorption and Photovoltaic Applications. *Biointerface Res. Appl. Chem.* **2021**, *12*, 3836–3848. [[CrossRef](#)]
16. Wang, W.; Tadé, M.O.; Shao, Z. Research Progress of Perovskite Materials in Photocatalysis- and Photovoltaics-Related Energy Conversion and Environmental Treatment. *Chem. Soc. Rev.* **2015**, *44*, 5371–5408. [[CrossRef](#)]
17. Gupta, A.; Zhang, R.; Kumar, P.; Kumar, V.; Kumar, A. Nano-Structured Dilute Magnetic Semiconductors for Efficient Spintronics at Room Temperature. *Magnetochemistry* **2020**, *6*, 15. [[CrossRef](#)]
18. Fajariah, N.; Prabowo, W.A.E.; Fathurrahman, F.; Melati, A.; Dipojono, H.K. The Investigation of Electronic Structure of Transition Metal Doped TiO<sub>2</sub> for Diluted Magnetic Semiconductor Applications: A First Principle Study. *Procedia Eng.* **2017**, *170*, 141–147. [[CrossRef](#)]
19. Parangi, T.; Kumar Mishra, M. Titanium Dioxide as Energy Storage Material: A Review on Recent Advancement. In *Titanium Dioxide*; IntechOpen: London, UK, 2021.
20. Wang, W.; Liu, Y.; Wu, X.; Wang, J.; Fu, L.; Zhu, Y.; Wu, Y.; Liu, X. Advances of TiO<sub>2</sub> as Negative Electrode Materials for Sodium-Ion Batteries. *Adv. Mater. Technol.* **2018**, *3*, 1800004. [[CrossRef](#)]
21. Zhang, H.; Banfield, J.F. Structural Characteristics and Mechanical and Thermodynamic Properties of Nanocrystalline TiO<sub>2</sub>. *Chem. Rev.* **2014**, *114*, 9613–9644. [[CrossRef](#)]
22. Sutrisno, H.; Sunarto, S. Polymorphic Transformation of Titanium Dioxide Caused by Heat Treatment of Protonic Lepidocrocite Titanate. *Indones. J. Chem.* **2010**, *10*, 143–148. [[CrossRef](#)]
23. Zhu, T.; Gao, S.-P. The Stability, Electronic Structure, and Optical Property of TiO<sub>2</sub> Polymorphs. *J. Phys. Chem. C* **2014**, *118*, 11385–11396. [[CrossRef](#)]
24. Mattesini, M.; de Almeida, J.S.; Dubrovinsky, L.; Dubrovinskaia, N.; Johansson, B.; Ahuja, R. Cubic TiO<sub>2</sub> as a Potential Light Absorber in Solar-Energy Conversion. *Phys. Rev. B* **2004**, *70*, 115101. [[CrossRef](#)]
25. Fehse, M.; Ventosa, E. Frontispiece: Is TiO<sub>2</sub> (B) the Future of Titanium-Based Battery Materials? *Chempluschem* **2015**, *80*, 785–795. [[CrossRef](#)] [[PubMed](#)]
26. Zukalová, M.; Kalbáč, M.; Kavan, L.; Exnar, I.; Graetzel, M.; Kalbáč, M.; Kavan, L.; Exnar, I.; Graetzel, M.; Kalbáč, M.; et al. Pseudocapacitive Lithium Storage in TiO<sub>2</sub>(B). *Chem. Mater.* **2005**, *17*, 1248–1255. [[CrossRef](#)]
27. Osman, S.; Peng, C.; Li, F.; Chen, H.; Shen, J.; Zhong, Z.; Huang, W.; Xue, D.; Liu, J. Defect-Induced Dense Amorphous/Crystalline Heterophase Enables High-Rate and Ultrastable Sodium Storage. *Adv. Sci.* **2022**, *9*, 2205575. [[CrossRef](#)] [[PubMed](#)]
28. Farooq, U.; Ahmed, F.; Pervez, S.A.; Rehman, S.; Pope, M.A.; Fichtner, M.; Roberts, E.P.L. A Stable TiO<sub>2</sub>–Graphene Nanocomposite Anode with High Rate Capability for Lithium-Ion Batteries. *RSC Adv.* **2020**, *10*, 29975–29982. [[CrossRef](#)]
29. Liao, C.; Li, F.; Liu, J. Challenges and Modification Strategies of Ni-Rich Cathode Materials Operating at High-Voltage. *Nanomaterials* **2022**, *12*, 1888. [[CrossRef](#)]
30. Sångeland, C.; Sun, B.; Brandell, D.; Berg, E.J.; Mindemark, J. Decomposition of Carbonate-Based Electrolytes: Differences and Peculiarities for Liquids vs. Polymers Observed Using Operando Gas Analysis. *Batter. Supercaps* **2021**, *4*, 785–790. [[CrossRef](#)]
31. Zhang, W.; Zhang, Y.; Yu, L.; Wu, N.-L.; Huang, H.; Wei, M. TiO<sub>2</sub>-B Nanowires via Topological Conversion with Enhanced Lithium-Ion Intercalation Properties. *J. Mater. Chem. A* **2019**, *7*, 3842–3847. [[CrossRef](#)]
32. Liu, J.; Li, P.; Li, F.; Liu, Z.; Xu, X.; Liu, J. Galvanic Replacement Preparation of Spindle-Structured Sb@C@NC as Anode for Superior Lithium-Ion Storage. *Batteries* **2022**, *8*, 245. [[CrossRef](#)]
33. Zeng, T.; Ji, P.; Shang, B.; Peng, Q.; Zhang, Y.; Hu, X. Electrochemical Performances of Carbon Coated FeSbO<sub>4</sub> as Anode Material for Lithium Batteries. *Mater. Lett.* **2017**, *201*, 198–202. [[CrossRef](#)]
34. Paul, S.; Rahman, M.A.; Sharif, S.B.; Kim, J.-H.; Siddiqui, S.-E.-T.; Hossain, M.A.M. TiO<sub>2</sub> as an Anode of High-Performance Lithium-Ion Batteries: A Comprehensive Review towards Practical Application. *Nanomaterials* **2022**, *12*, 2034. [[CrossRef](#)] [[PubMed](#)]
35. Schweidler, S.; de Biasi, L.; Schiele, A.; Hartmann, P.; Brezesinski, T.; Janek, J. Volume Changes of Graphite Anodes Revisited: A Combined Operando X-ray Diffraction and In Situ Pressure Analysis Study. *J. Phys. Chem. C* **2018**, *122*, 8829–8835. [[CrossRef](#)]

36. Cai, J.; Wang, Y.; Zhu, Y.; Wu, M.; Zhang, H.; Li, X.; Jiang, Z.; Meng, M. In Situ Formation of Disorder-Engineered TiO<sub>2</sub>(B)-Anatase Heterophase Junction for Enhanced Photocatalytic Hydrogen Evolution. *ACS Appl. Mater. Interfaces* **2015**, *7*, 24987–24992. [[CrossRef](#)]
37. Yin, S.; Wu, J.; Aki, M.; Sato, T. Photocatalytic Hydrogen Evolution with Fibrous Titania Prepared by the Solvothermal Reactions of Protonic Layered Tetratitanate (H<sub>2</sub>Ti<sub>4</sub>O<sub>9</sub>). *Int. J. Inorg. Mater.* **2000**, *2*, 325–331. [[CrossRef](#)]
38. Grosjean, R.; Fehse, M.; Pigeot-Remy, S.; Stievano, L.; Monconduit, L.; Cassaignon, S. Facile Synthetic Route towards Nanostructured Fe-TiO<sub>2</sub>(B), Used as Negative Electrode for Li-Ion Batteries. *J. Power Sources* **2015**, *278*, 1–8. [[CrossRef](#)]
39. Zhang, K.; Katz, M.B.; Li, B.; Kim, S.J.; Du, X.; Hao, X.; Jokisaari, J.R.; Zhang, S.; Graham, G.W.; Van der Ven, A.; et al. Water-Free Titania-Bronze Thin Films with Superfast Lithium-Ion Transport. *Adv. Mater.* **2014**, *26*, 7365–7370. [[CrossRef](#)]
40. Zhang, Y.; Meng, Y.; Zhu, K.; Qiu, H.; Ju, Y.; Gao, Y.; Du, F.; Zou, B.; Chen, G.; Wei, Y. Copper-Doped Titanium Dioxide Bronze Nanowires with Superior High Rate Capability for Lithium Ion Batteries. *ACS Appl. Mater. Interfaces* **2016**, *8*, 7957–7965. [[CrossRef](#)]
41. Opra, D.P.; Gnedenkov, S.V.; Sinebryukhov, S.L.; Gerasimenko, A.V.; Ziatdinov, A.M.; Sokolov, A.A.; Podgorbunsky, A.B.; Ustinov, A.Y.; Kuryavyi, V.G.; Mayorov, V.Y.; et al. Enhancing Lithium and Sodium Storage Properties of TiO<sub>2</sub>(B) Nanobelts by Doping with Nickel and Zinc. *Nanomaterials* **2021**, *11*, 1703. [[CrossRef](#)]
42. Opra, D.P.; Gnedenkov, S.V.; Sokolov, A.A.; Podgorbunsky, A.B.; Ustinov, A.Y.; Mayorov, V.Y.; Kuryavyi, V.G.; Sinebryukhov, S.L. Vanadium-Doped TiO<sub>2</sub>-B/Anatase Mesoporous Nanotubes with Improved Rate and Cycle Performance for Rechargeable Lithium and Sodium Batteries. *J. Mater. Sci. Technol.* **2020**, *54*, 181–189. [[CrossRef](#)]
43. Amirsalehi, M.; Askari, M. Influence of Vanadium, Cobalt-Codoping on Electrochemical Performance of Titanium Dioxide Bronze Nanobelts Used as Lithium Ion Battery Anodes. *J. Mater. Sci. Mater. Electron.* **2018**, *29*, 13068–13076. [[CrossRef](#)]
44. Cao, M.; Tao, L.; Lv, X.; Bu, Y.; Li, M.; Yin, H.; Zhu, M.; Zhong, Z.; Shen, Y.; Wang, M. Phosphorus-Doped TiO<sub>2</sub>-B Nanowire Arrays Boosting Robust Pseudocapacitive Properties for Lithium Storage. *J. Power Sources* **2018**, *396*, 327–334. [[CrossRef](#)]
45. Han, Z.; Peng, J.; Liu, L.; Wang, G.; Yu, F.; Guo, X. Few-Layer TiO<sub>2</sub>-B Nanosheets with N-Doped Graphene Nanosheets as a Highly Robust Anode for Lithium-Ion Batteries. *RSC Adv.* **2017**, *7*, 7864–7869. [[CrossRef](#)]
46. Chen, C.; Hu, X.; Zhang, B.; Miao, L.; Huang, Y. Architectural Design and Phase Engineering of N/B-Codoped TiO<sub>2</sub>(B)/Anatase Nanotube Assemblies for High-Rate and Long-Life Lithium Storage. *J. Mater. Chem. A* **2015**, *3*, 22591–22598. [[CrossRef](#)]
47. Ventosa, E.; Mei, B.; Xia, W.; Muhler, M.; Schuhmann, W. TiO<sub>2</sub>(B)/Anatase Composites Synthesized by Spray Drying as High Performance Negative Electrode Material in Li-Ion Batteries. *ChemSusChem* **2013**, *6*, 1312–1315. [[CrossRef](#)]
48. Goriparti, S.; Miele, E.; Prato, M.; Scarpellini, A.; Marras, S.; Monaco, S.; Toma, A.; Messina, G.C.; Alabastri, A.; de Angelis, F.; et al. Direct Synthesis of Carbon-Doped TiO<sub>2</sub>-Bronze Nanowires as Anode Materials for High Performance Lithium-Ion Batteries. *ACS Appl. Mater. Interfaces* **2015**, *7*, 25139–25146. [[CrossRef](#)]
49. Li, Y.; Shen, J.; Li, J.; Liu, S.; Yu, D.; Xu, R.; Fu, W.-F.; Lv, X.-J. Constructing a Novel Strategy for Carbon-Doped TiO<sub>2</sub> Multiple-Phase Nanocomposites toward Superior Electrochemical Performance for Lithium Ion Batteries and the Hydrogen Evolution Reaction. *J. Mater. Chem. A* **2017**, *5*, 7055–7063. [[CrossRef](#)]
50. Hasegawa, G.; Tanaka, M.; Vequizo, J.J.M.; Yamakata, A.; Hojo, H.; Kobayashi, M.; Kakihana, M.; Inada, M.; Akamatsu, H.; Hayashi, K. Sodium Titanium Oxide Bronze Nanoparticles Synthesized via Concurrent Reduction and Na<sup>+</sup>-Doping into TiO<sub>2</sub>(B). *Nanoscale* **2019**, *11*, 1442–1450. [[CrossRef](#)]
51. Su, J.; Li, Z.; Zhang, Y.; Wei, Y.; Wang, X. N-Doped and Cu-Doped TiO<sub>2</sub>-B Nanowires with Enhanced Photoelectrochemical Activity. *RSC Adv.* **2016**, *6*, 16177–16182. [[CrossRef](#)]
52. Zhang, Z.; Zhou, Z.; Nie, S.; Wang, H.; Peng, H.; Li, G.; Chen, K. Flower-like Hydrogenated TiO<sub>2</sub>(B) Nanostructures as Anode Materials for High-Performance Lithium Ion Batteries. *J. Power Sources* **2014**, *267*, 388–393. [[CrossRef](#)]
53. Song, W.; Chen, J.; Ji, X.; Zhang, X.; Xie, F.; Riley, D.J. Dandelion-Shaped TiO<sub>2</sub>/Multi-Layer Graphene Composed of TiO<sub>2</sub>(B) Fibrils and Anatase TiO<sub>2</sub> Pappi Utilizing Triphase Boundaries for Lithium Storage. *J. Mater. Chem. A* **2016**, *4*, 8762–8768. [[CrossRef](#)]
54. Petříček, V.; Dušek, M.; Palatinus, L. Crystallographic Computing System JANA2006: General Features. *Z. Für Krist. Cryst. Mater.* **2014**, *229*, 345–352. [[CrossRef](#)]
55. Autthawong, T.; Chimupala, Y.; Haruta, M.; Kurata, H.; Kiyomura, T.; Yu, A.; Chairuangstri, T.; Sarakonsri, T. Ultrafast-Charging and Long Cycle-Life Anode Materials of TiO<sub>2</sub>-Bronze/Nitrogen-Doped Graphene Nanocomposites for High-Performance Lithium-Ion Batteries. *RSC Adv.* **2020**, *10*, 43811–43824. [[CrossRef](#)]
56. Moreira, A.J.; Malafatti, J.O.D.; Giraldo, T.R.; Paris, E.C.; Pereira, E.C.; de Mendonça, V.R.; Mastelaro, V.R.; Freschi, G.P.G. Prozac<sup>®</sup> Photodegradation Mediated by Mn-Doped TiO<sub>2</sub> Nanoparticles: Evaluation of by-Products and Mechanisms Proposal. *J. Environ. Chem. Eng.* **2020**, *8*, 104543. [[CrossRef](#)]
57. Birlik, I.; Dagdelen, D. Synergistic Effect of Manganese and Nitrogen Codoping on Photocatalytic Properties of Titania Nanoparticles. *Bull. Mater. Sci.* **2020**, *43*, 85. [[CrossRef](#)]
58. Huang, Z.; Hu, L.; Zhou, Q.; Guo, Y.; Tang, W.; Dai, J. Effect of Aging on Surface Chemistry of Rice Husk-Derived Biochar. *Environ. Prog. Sustain. Energy* **2018**, *37*, 410–417. [[CrossRef](#)]
59. Singh, A.P.; Wang, R.B.; Tossi, C.; Tittonen, I.; Wickman, B.; Hellman, A. Hydrogen Induced Interface Engineering in Fe<sub>2</sub>O<sub>3</sub>-TiO<sub>2</sub> Heterostructures for Efficient Charge Separation for Solar-Driven Water Oxidation in Photoelectrochemical Cells. *RSC Adv.* **2021**, *11*, 4297–4307. [[CrossRef](#)] [[PubMed](#)]

60. Guo, M.; Gao, Y.; Shao, G. Complex Doping Chemistry Owing to Mn Incorporation in Nanocrystalline Anatase TiO<sub>2</sub> Powders. *Phys. Chem. Chem. Phys.* **2016**, *18*, 2818–2829. [[CrossRef](#)]
61. Zhou, J.K.; Lv, L.; Yu, J.; Li, H.L.; Guo, P.-Z.; Sun, H.; Zhao, X.S. Synthesis of Self-Organized Polycrystalline F-Doped TiO<sub>2</sub> Hollow Microspheres and Their Photocatalytic Activity under Visible Light. *J. Phys. Chem. C* **2008**, *112*, 5316–5321. [[CrossRef](#)]
62. Yu, J.C.; Yu, J.; Ho, W.; Jiang, Z.; Zhang, L. Effects of F-Doping on the Photocatalytic Activity and Microstructures of Nanocrystalline TiO<sub>2</sub> Powders. *Chem. Mater.* **2002**, *14*, 3808–3816. [[CrossRef](#)]
63. Viswanathan, B.; Krishnamurthy, K.R. Nitrogen Incorporation in TiO<sub>2</sub>: Does It Make a Visible Light Photo-Active Material? *Int. J. Photoenergy* **2012**, *2012*, 269654. [[CrossRef](#)]
64. Lee, S.; Cho, I.-S.; Lee, D.K.; Kim, D.W.; Noh, T.H.; Kwak, C.H.; Park, S.; Hong, K.S.; Lee, J.-K.; Jung, H.S. Influence of Nitrogen Chemical States on Photocatalytic Activities of Nitrogen-Doped TiO<sub>2</sub> Nanoparticles under Visible Light. *J. Photochem. Photobiol. A Chem.* **2010**, *213*, 129–135. [[CrossRef](#)]
65. Lei, Y.; Li, J.; Wang, Z.; Sun, J.; Chen, F.; Liu, H.; Ma, X.; Liu, Z. Atomic-Scale Investigation of a New Phase Transformation Process in TiO<sub>2</sub> Nanofibers. *Nanoscale* **2017**, *9*, 4601–4609. [[CrossRef](#)] [[PubMed](#)]
66. Cai, Y.; Wang, H.-E.; Huang, S.-Z.; Jin, J.; Wang, C.; Yu, Y.; Li, Y.; Su, B.-L. Hierarchical Nanotube-Constructed Porous TiO<sub>2</sub>-B Spheres for High Performance Lithium Ion Batteries. *Sci. Rep.* **2015**, *5*, 11557. [[CrossRef](#)] [[PubMed](#)]
67. Qu, J.; Cloud, J.E.; Yang, Y.; Ding, J.; Yuan, N. Synthesis of Nanoparticles-Deposited Double-Walled TiO<sub>2</sub>-B Nanotubes with Enhanced Performance for Lithium-Ion Batteries. *ACS Appl. Mater. Interfaces* **2014**, *6*, 22199–22208. [[CrossRef](#)] [[PubMed](#)]
68. Hu, H.; Yu, L.; Gao, X.; Lin, Z.; Lou, X.W. Hierarchical Tubular Structures Constructed from Ultrathin TiO<sub>2</sub>(B) Nanosheets for Highly Reversible Lithium Storage. *Energy Environ. Sci.* **2015**, *8*, 1480–1483. [[CrossRef](#)]
69. Li, X.; Li, M.; Liang, J.; Wang, X.; Yu, K. Growth Mechanism of Hollow TiO<sub>2</sub>(B) Nanocrystals as Powerful Application in Lithium-Ion Batteries. *J. Alloys Compd.* **2016**, *681*, 471–476. [[CrossRef](#)]
70. Banerjee, D.; Gupta, S.K.; Patra, N.; Raja, S.W.; Pathak, N.; Bhattacharyya, D.; Pujari, P.K.; Thakare, S.V.; Jha, S.N. Unraveling Doping Induced Anatase–Rutile Phase Transition in TiO<sub>2</sub> Using Electron, X-ray and Gamma-ray as Spectroscopic Probes. *Phys. Chem. Chem. Phys.* **2018**, *20*, 28699–28711. [[CrossRef](#)]
71. Lin, Y.-W. *Cation-Doped Titania Thin Films*; University of New South Wales: Sydney, Australia, 2015.
72. Borkar, S.A.; Dharwadkar, S.R. Temperatures and Kinetics of Anatase to Rutile Transformation in Doped TiO<sub>2</sub> Heated in Microwave Field. *J. Therm. Anal. Calorim.* **2004**, *78*, 761–767. [[CrossRef](#)]
73. Arroyo, R.; Córdoba, G.; Padilla, J.; Lara, V. Influence of Manganese Ions on the Anatase–Rutile Phase Transition of TiO<sub>2</sub> Prepared by the Sol–Gel Process. *Mater. Lett.* **2002**, *54*, 397–402. [[CrossRef](#)]
74. Lee, H.B.; Ginting, R.T.; Tan, S.T.; Tan, C.H.; Alshangleh, A.; Oleiwi, H.F.; Yap, C.C.; Jumali, M.H.H.; Yahaya, M. Controlled Defects of Fluorine-Incorporated ZnO Nanorods for Photovoltaic Enhancement. *Sci. Rep.* **2016**, *6*, 32645. [[CrossRef](#)] [[PubMed](#)]
75. Hanaor, D.A.H.A.H.; Sorrell, C.C.C. Review of the Anatase to Rutile Phase Transformation. *J. Mater. Sci.* **2011**, *46*, 855–874. [[CrossRef](#)]
76. Lv, K.; Xiang, Q.; Yu, J. Effect of Calcination Temperature on Morphology and Photocatalytic Activity of Anatase TiO<sub>2</sub> Nanosheets with Exposed {0 0 1} Facets. *Appl. Catal. B Environ.* **2011**, *104*, 275–281. [[CrossRef](#)]
77. Jin, J.; Wu, L.; Huang, S.; Yan, M.; Wang, H.; Chen, L.; Hasan, T.; Li, Y.; Su, B.-L. Hierarchy Design in Metal Oxides as Anodes for Advanced Lithium-Ion Batteries. *Small Methods* **2018**, *2*, 1800171. [[CrossRef](#)]
78. Kolesnik, I.V.; Lebedev, V.A.; Garshev, A.V. Optical Properties and Photocatalytic Activity of Nanocrystalline TiO<sub>2</sub> Doped by 3d-Metal Ions. *Nanosyst. Phys. Chem. Math.* **2018**, *9*, 401–409. [[CrossRef](#)]
79. Smirnova, N.; Petrik, I.; Vorobets, V.; Kolbasov, G.; Eremenko, A. Sol-Gel Synthesis, Photo- and Electrochemical Properties of Mesoporous TiO<sub>2</sub> Modified with Transition Metal Ions. *Nanoscale Res. Lett.* **2017**, *12*, 239. [[CrossRef](#)]
80. Kijlstra, W.S.; Poels, E.K.; Blik, A.; Weckhuysen, B.M.; Schoonheydt, R.A. Characterization of Al<sub>2</sub>O<sub>3</sub>-Supported Manganese Oxides by Electron Spin Resonance and Diffuse Reflectance Spectroscopy. *J. Phys. Chem. B* **1997**, *101*, 309–316. [[CrossRef](#)]
81. Zhang, D.-A.; Wang, Q.; Wang, Q.; Sun, J.; Xing, L.-L.; Xue, X.-Y. Core–Shell SnO<sub>2</sub>@TiO<sub>2</sub>-B Nanowires as the Anode of Lithium Ion Battery with High Capacity and Rate Capability. *Mater. Lett.* **2014**, *128*, 295–298. [[CrossRef](#)]
82. Du, S.; Lian, J.; Zhang, F. Visible Light-Responsive N-Doped TiO<sub>2</sub> Photocatalysis: Synthesis, Characterizations, and Applications. *Trans. Tianjin Univ.* **2022**, *28*, 33–52. [[CrossRef](#)]
83. Dozzi, M.V.; Selli, E. Doping TiO<sub>2</sub> with P-Block Elements: Effects on Photocatalytic Activity. *J. Photochem. Photobiol. C Photochem. Rev.* **2013**, *14*, 13–28. [[CrossRef](#)]
84. Zhao, H.; Pan, F.; Li, Y. A Review on the Effects of TiO<sub>2</sub> Surface Point Defects on CO<sub>2</sub> Photoreduction with H<sub>2</sub>O. *J. Mater.* **2017**, *3*, 17–32. [[CrossRef](#)]
85. Cheng, X.; Yu, X.; Xing, Z.; Yang, L. Synthesis and Characterization of N-Doped TiO<sub>2</sub> and Its Enhanced Visible-Light Photocatalytic Activity. *Arab. J. Chem.* **2016**, *9*, S1706–S1711. [[CrossRef](#)]
86. Feng, N.; Liu, F.; Huang, M.; Zheng, A.; Wang, Q.; Chen, T.; Cao, G.; Xu, J.; Fan, J.; Deng, F. Unravelling the Efficient Photocatalytic Activity of Boron-Induced Ti<sup>3+</sup> Species in the Surface Layer of TiO<sub>2</sub>. *Sci. Rep.* **2016**, *6*, 34765. [[CrossRef](#)] [[PubMed](#)]
87. Marques, F.C.; Jasieniak, J.J. Ionization Potential and Electron Attenuation Length of Titanium Dioxide Deposited by Atomic Layer Deposition Determined by Photoelectron Spectroscopy in Air. *Appl. Surf. Sci.* **2017**, *422*, 504–508. [[CrossRef](#)]
88. Umek, P.; Bittencourt, C.; Guttman, P.; Gloter, A.; Škapin, S.D.; Arçon, D. Mn<sup>2+</sup> Substitutional Doping of TiO<sub>2</sub> Nanoribbons: A Three-Step Approach. *J. Phys. Chem. C* **2014**, *118*, 21250–21257. [[CrossRef](#)]

89. Popa, A.; Raita, O.; Stan, M.; Pana, O.; Borodi, G.; Giurgiu, L.M. Electron Paramagnetic Resonance of Mn-Doped  $\text{Sn}_{1-x}\text{Mn}_x\text{O}_2$  Powders. *Appl. Magn. Reson.* **2012**, *42*, 453–462. [[CrossRef](#)]
90. Güler, S.; Rameev, B.; Khaibullin, R.I.; Lopatin, O.N.; Aktaş, B. EPR Study of Mn-Implanted Single Crystal Plates of  $\text{TiO}_2$  Rutile. *J. Magn. Magn. Mater.* **2010**, *322*, L13–L17. [[CrossRef](#)]
91. Sakaguchi Miyamoto, N.; Miyamoto, R.; Giamello, E.; Kurisaki, T.; Wakita, H. Evaluation of Coexistent Metal Ions with  $\text{TiO}_2$ : An EPR Approach. *Res. Chem. Intermed.* **2018**, *44*, 4563–4575. [[CrossRef](#)]
92. Müller, K.A. Electron Paramagnetic Resonance of Manganese IV in  $\text{SrTiO}_3$ . *Phys. Rev. Lett.* **1959**, *2*, 341–343. [[CrossRef](#)]
93. Castner, T.; Newell, G.S.; Holton, W.C.; Slichter, C.P. Note on the Paramagnetic Resonance of Iron in Glass. *J. Chem. Phys.* **1960**, *32*, 668–673. [[CrossRef](#)]
94. Griscom, D.L.; Griscom, R.E. Paramagnetic Resonance of  $\text{Mn}^{2+}$  in Glasses and Compounds of the Lithium Borate System. *J. Chem. Phys.* **1967**, *47*, 2711–2722. [[CrossRef](#)]
95. Brutti, S.; Gentili, V.; Reale, P.; Carbone, L.; Panero, S. Mitigation of the Irreversible Capacity and Electrolyte Decomposition in a  $\text{LiNi}_{0.5}\text{Mn}_{1.5}\text{O}_4$ /Nano- $\text{TiO}_2$  Li-Ion Battery. *J. Power Sources* **2011**, *196*, 9792–9799. [[CrossRef](#)]
96. Dylla, A.G.; Henkelman, G.; Stevenson, K.J. Lithium Insertion in Nanostructured  $\text{TiO}_2(\text{B})$  Architectures. *Acc. Chem. Res.* **2013**, *46*, 1104–1112. [[CrossRef](#)] [[PubMed](#)]
97. Aurbach, D.; Talyosef, Y.; Markovsky, B.; Markevich, E.; Zinigrad, E.; Asraf, L.; Gnanaraj, J.S.; Kim, H.-J. Design of Electrolyte Solutions for Li and Li-Ion Batteries: A Review. *Electrochim. Acta* **2004**, *50*, 247–254. [[CrossRef](#)]
98. Xia, L.; Yu, L.; Hu, D.; Chen, G.Z. Electrolytes for Electrochemical Energy Storage. *Mater. Chem. Front.* **2017**, *1*, 584–618. [[CrossRef](#)]
99. Kavan, L. Electrochemistry of Titanium Dioxide: Some Aspects and Highlights. *Chem. Rec.* **2012**, *12*, 131–142. [[CrossRef](#)]
100. Zhang, Y.; Fu, Q.; Xu, Q.; Yan, X.; Zhang, R.; Guo, Z.; Du, F.; Wei, Y.; Zhang, D.; Chen, G. Improved Electrochemical Performance of Nitrogen Doped  $\text{TiO}_2\text{-B}$  Nanowires as Anode Materials for Li-Ion Batteries. *Nanoscale* **2015**, *7*, 12215–12224. [[CrossRef](#)]
101. Armstrong, G.; Armstrong, A.R.; Bruce, P.G.; Reale, P.; Scrosati, B.  $\text{TiO}_2(\text{B})$  Nanowires as an Improved Anode Material for Lithium-Ion Batteries Containing  $\text{LiFePO}_4$  or  $\text{LiNi}_{0.5}\text{Mn}_{1.5}\text{O}_4$  Cathodes and a Polymer Electrolyte. *Adv. Mater.* **2006**, *18*, 2597–2600. [[CrossRef](#)]
102. Wang, L.; Zuo, P.; Yin, G.; Ma, Y.; Cheng, X.; Du, C.; Gao, Y. Improved Electrochemical Performance and Capacity Fading Mechanism of Nano-Sized  $\text{LiMn}_{0.9}\text{Fe}_{0.1}\text{PO}_4$  Cathode Modified by Polyacene Coating. *J. Mater. Chem. A* **2015**, *3*, 1569–1579. [[CrossRef](#)]

**Disclaimer/Publisher’s Note:** The statements, opinions and data contained in all publications are solely those of the individual author(s) and contributor(s) and not of MDPI and/or the editor(s). MDPI and/or the editor(s) disclaim responsibility for any injury to people or property resulting from any ideas, methods, instructions or products referred to in the content.